Winter 11-2012

Transport of Engineered Nanomaterials in Porous Media: Groundwater Remediation Application and Effects of Particle Shape

Megan Seymour
University of Nebraska-Lincoln, megan.seymour@hotmail.com

TRANSPORT OF ENGINEERED NANOMATERIALS IN POROUS MEDIA: GROUNDWATER REMEDIATION APPLICATION AND EFFECTS OF PARTICLE SHAPE

By

Megan Seymour

A THESIS

Presented to the Faculty of
The Graduate College at the University of Nebraska
In Partial Fulfillment of the Requirements
For the Degree of Master Of Science

Major: Environmental Engineering

Under the Supervision of Professor Yusong Li

Lincoln, Nebraska

November, 2012

TRANSPORT OF ENGINEERED NANOMATERIALS IN POROUS MEDIA: GROUNDWATER REMEDIATION APPLICATION AND EFFECTS OF PARTICLE SHAPE

Megan Seymour, M.S.

University of Nebraska, 2012

Advisor: Yusong Li

Nanotechnology, referring to any science which utilizes particles at the nanoscale, has substantially grown in recent years for its wide spectrum of potential uses. Many theories and models have been developed around the transport of spherical particles; however nanoparticles can be found in various shapes which could greatly affect the predicted transport and retention in the subsurface.

This research explores the beneficial use of carbon nano-onions (CNOs) for environmental remediation and investigates the transport of CNOs in saturated porous media. Surface oxidized CNOs possessed 10 times higher sorption capacity compared to C_{60} for heavy metal ions including Pb^{2+}, Cu^{2+}, Cd^{2+}, Ni^{2+}, and Zn^{2+}. CNOs aqueous suspension can be very stable in NaCl solution at ionic strength up to 30 mM and $CaCl_2$ solution up to 4 mM $CaCl_2$ when pH ranged from 5 to 9, consistent with environmental relevant conditions. Interactions of CNOs with iron oxide and silica surfaces under favorable condition were found to be electrostatic in origin. Mobility of CNOs in quartz sands was controlled by electrolyte type and concentration. Approximately 4.4%, 25.1%, and 92.5% of injected CNO mass were retained in the sand column in ultrapure water, 1 mM NaCl, and 1 mM $CaCl_2$ solutions, respectively.

The second part of this research explored the influence of nanoparticle shape on the transport and retention. Spherical polystyrene nanoparticles were stretched into rod shapes with either 2:1 or 4:1 aspect ratio. Using Quartz Crystal Microbalance with Dissipation (QCM-D) particle deposition experiments, spherical particles displayed a higher deposition rate compared to rod-shape under favorable conditions. The rod-shape particles were all insensitive to changes in ionic strengths of 10 to 100 mM NaCl. Transport and deposition in saturated porous media was investigated by microfluidic flow cell experiments incorporated with Laser Scanning Cytometry (LSC). Results showed higher attachment rate for rod-shape particles compared to spherical. It was also determined that physical and chemical surface heterogeneity plays a significant role in the observed attachment onto the glass beads.

Acknowledgements

As this journey draws to an end, I would like to express my appreciation to those individuals that have helped me with their support and guidance. First, I would whole heartily like to express my thanks to Jeffrey, my loving husband. Without his support and love, this journey would have been much more difficult. He was always there with patience, an open ear, and encouraging words.

I am also very grateful to my advisor, Dr. Yusong Li, for her constant faith in my ability. I appreciate the wonderful opportunity she has given me to believe in myself and accomplish something at one point I never thought possible. She has provided me with this valuable opportunity, and for that I am deeply thankful for her support.

I would like to express my gratitude towards my family and friends, who have been very patient and understanding throughout the last two years. I also wish to thank my fellow research group members Ryan May, Chunmei Bai, Simin Akbariyeh, and Negin Kananizadeh for their help and support. Thank you to Kat Camancho at University of California-Santa Barbara for taking the time to teach me how to stretch nanoparticles. Thanks also to Alexander Goponenko in the Biomechanics, Biomaterials and Biomedicine Instrumentation Facility (BM^3) for their support and facility use. Thank you to my committee members, Dr. Xu Li and Dr. Shannon Bartlet-Hunt for their support.

Sincere thanks are also due to Dr. Chunming Su, Dr. Gexin Chen, Dr. Xuyang Liu, and Marc Banworth, at the U.S. EPA, for all of their assistance and the opportunity to work at the EPA laboratory in Ada, Oklahoma. Last but not least, a very kind thank you is due to my dear friend Susan Mravik who opened her home to me in Oklahoma.

Table of Contents

List of Tables

Chapter 2

Chapter 4

List of Figures

Chapter 2

Chapter 3

Chapter 4

CHAPTER 1

PROJECT OVERIVEW AND OBJECTIVES

1.0 Project Overview

The area of nanotechnology is one of the most active research areas in science in recent years. Nanoparticles have exhibited new or improved properties due to their unique small size and various shapes. Nanotechnology applications can vary from areas of medicine, manufacturing, energy production, and environmental applications. There are an estimated 294,000 hazardous waste sites in the U.S., which may require $373 billion to $1694 trillion dollars to clean up (Burroughs, 2000). A potential use of nanotechnology could be utilized for chemical and physical processes for remediation of toxic chemicals in the subsurface.

Carbonaceous nanomaterials, such as fullerene C_{60} and carbon nanotubes (CNTs), have demonstrated to possess high sorption capacity (Mauter and Elimelech, 2008). Studies found C_{60} was able to adsorb a high amount of organic contaminants and CNTs with surface modifications have a high capacity for sorption of heavy metals (Yang et al., 2006 & Li et al. 2003). Although both these nanoparticles could hold promise for new remediation technologies, the major challenge faced before actual operation is the cost of materials. Unfortunately, both CNTs and C_{60} are extremely expensive to produce and use in field applications. However, a new member of the carbonaceous family known as carbon nano-onions (CNOs) was discovered in 1992 by Daniel Ugarte (Ugarte 1993). With recently developed and newly cost-effective production of CNOs, remediation applications utilizing CNOs could be feasible (Gao et al., 2011).

Although nanoparticle applications have great potential, there are unknown behaviors of these particles once released into the environment. Knowledge of the fate and transport of nanoparticles in porous media is required to further explore the beneficial uses of nanotechnology and to prevent unintended exposures to the environment. Compared to colloids or other emerging contaminants, nanoparticles pose new challenges for scientists. Engineered and naturally occurring nanoparticles can be found in various shapes, for example, carbon nanotubes have a high aspect ratio (Lecoanet et al., 2004). It is already obvious that particle size and environmental conditions plays an important role in the transport and deposition of both colloids and nanoparticles (Wang et al., 2012 and Lecoanet et. al., 2004), but the role particle shape plays on nanoparticle transport in the environment is less understood. A few previous studies have explored colloid transport and the influence of shape, and found particles with higher aspect ratios displayed greater retention (Salerno et al., 2006 and Liu et al., 2010). However studies by Xu et al. (2008) concluded the retention was not affected by rod-shape particles when compared to spherical. Therefore more research on the effect of particle shape on transport and retention at the nano-scale is warranted.

Historically, column studies have provided important insights into the retention of nanoparticles in model porous media such as glass beads or Ottawa sands; however, these experiments cannot directly observe the spatial attachment of nanoparticles on collector surfaces. Recently, the technique of using laser scanning cytometry (LSC) has shown to provide the spatial distribution of nanoscale particles in porous media over several pore volumes (May et al., 2012). This technique can prove to be effective in understanding the retention of various shaped nanoparticles in saturated flow conditions.

2.0 Objectives

The overall objectives of this study include two different but related aspects:

1. Understand the beneficial use of carbon nano-onions for heavy metal ion remediation based on their sorption capacity to various heavy metal ions and mobility in saturated porous media under environmentally relevant conditions.
2. Explore the influences of particles shape on the transport and retentions of nano-scale particles using LSC incorporated microfluidic flow cell experiments and and QCM-D experiments.

3.0 Thesis Organization

This thesis is organized in the following way. The Chapter 3 provides a background review on the nanotechnology, their environmental application, and fate and transport of nanomaterials in porous media. Chapter 4 addresses the first objective, i.e. characterization of CNOs for heavy metal ion remediation. This part of work has already been published in the Journal of Nanoparticle Research (DOI 10.1007/s11051-012-1087-y). Chapter 5 addresses the second objective, i.e. the role of nanoparticle shape on their transport. A journal paper is under preparation based on this part of work. Finally, detailed experimental procedures and additional experimental data are included in an appendix at the end of the thesis.

References

Burroughs, C., 2000. Sandia scientists study 'natural' alternative to cleaning up uranium contaminated sites: natural attenuation may replace costly traditional remediation techniques. Sandia Lab News, Sandia.

Gao, Y., Zhou, Y. S., Park, J. B., Wang, H., He, X. N., Luo, H. F., Jiang, L., Lu, Y. F., 2011. Resonant excitation of precursor molecules in improving the particle crystallinity, growth rate and optical limiting performance of carbon nano-onions. Nanotechnology 22, 165604.

Lecoanet, H. F., Bottero, J., Wiesner, M. R., 2004. Laboratory assessment of the mobility of nanomaterials in porous media. Environ. Sci. Technol. 38 (19), 5164-5169.

Li, Y. H., Wang, S. G., Luan, Z. K., Ding, J., Xu, C. L., Wu, D. H., 2003. Adsorption of cadmium(II) from aqueous solution by surface oxidized carbon nanotubes. Carbon 41 (5), 1057-1062.

Liu, Q., Lazouskaya, V., He, Q., Jin, Y., 2010. Effect of particle shape on colloid retention and release in saturated porous media. Journal of Environmental Quality 39, 500-508.

Mauter, M. S., Elimelech, M., 2008. Environmental applications of carbon-based nanomaterials. Environ. Sci. Technol. 42 (16), 5843-5859.

May, R., Akbariyeh, S., Li, Y., 2012. Pore-scale investigation of nanoparticle transport in saturated porous media using laser scanning cytometry. Environ. Sci. Technol. 46 (18), 9980-9986.

Salerno, M. B., Flamm, M., Logan, B. E., Velegol, D., 2006. Transport of rodlike colloids through packed beds. Environ. Sci. Technol. 40 (20), 6336-6340.

Ugarte, D., 1993. Formation mechanism of quasi-spherical carbon particles induced by electron bombardment. Chem. Phys. Lett. 207 (4-6), 473-479.

Wang, C., Bobba, A. D., Attinti, R., Shen, C., Lazouskaya, V., Wang, L., Jin, Y., 2012. Retention and transport of silica nanoparticles in saturated porous media: effect of concentration and particle size. Environ. Sci. Technol. 46 (13), 7151-7158.

Xu, S., Liao, Q., Saiers, J. E., 2008. Straining of nonspherical colloids in saturated porous media. Environ. Sci. Technol. 42 (3), 771-778.

Yang, K., Zhu, L. Z., Xing, B. S., 2006. Adsorption of polycyclic aromatic hydrocarbons by carbon nanomaterials. Environ. Sci. Technol. 40 (6), 1855-1861.

CHAPTER 2

BACKGROUND

1.0 Introduction to Nanotechnology

Nanotechnology, although the concept was raised over 50 years ago, has gained a lot of attention in the field of science and engineering in most recent years. Originally, physicist Richard Feynman delivered a talk in 1959 outlining the potential of nanotechnology entitled "There is Plenty Room at the Bottom" (Hickman, 2002). Since then, the field of nanotechnology has grown to be a feasible application to many disciplines such as medicine and health, electronics, manufacturing, energy production, industry, and environmental applications. The increase in the interest and applications of nanomaterials has grown vastly due to the new ability to observe and research these materials at a very small scale with the use of sophisticated tools such as electron microscopy.

A nanomaterial is defined as particles having a least one dimension in the range of 1 to 100 nm, which can be comparable to $1/80^{th,}$ the diameter of a human hair (National Nanotechnology Initiative). These extremely small sizes and unique properties are what make nanoparticles a promising application for science. Several medical studies have been conducted on the use of nanoparticles for drug delivery, gene therapy, and medical diagnostics (Hickman, 2002). Other areas of science have also taken advantage of the unique properties of nano-sized particle and are described in Table 1.

Table 1. Current applications of nanotechnology in industry.

Industry	Uses
Manufacturing	Plastic nanocomposite used to make car bumpers that are scratch-resistant, light-weight, and rust-proof Nano-cement used as tough, durable, high temperature fire protection coating on steel
Energy	Gel-based nanoscale catalyst used to liquefy coal and convert to gasoline or diesel Nanoparticles used to increase surface area of solar panel cells, thus increasing efficiency
Environmental	Nanofiltration products used to filter out nano-sized particles from drinking water Nanoparticles used in remediation technologies to increase surface area exposed to contaminants
Electronics	Nanostructured polymer films used in LED screens on phones Carbon nanotubes used to construct memory storage devices
Medical	Nanoparticles in sunscreen used to absorb UV light Nanoparticles used to deliver drugs to specific cells in the body Nanotubes used as scaffolding to help regrow bones and tissue
Aeronautics	Aluminum nanoparticles used in rocket propellant that burns at double the rate Nanotechnology used to produce lighter and stronger materials will help reduce fuel consumption

Source: Contents obtained from (Nanotechnology Now, 2012; Understanding Nanotechnology, 2007; Lofgren, 2005; and Mann, 2006).

2.0 Environmental Applications

Nanotechnology can be beneficial for chemical and physical processes of groundwater remediation of toxic chemicals in the subsurface. There is a need to improve the efficiency of remediation technologies already present, and to possibly design new treatment processes. The advantage of the nano-sized particles could provide some solutions for the increasing need to remediate contaminated groundwater and soil. For example, the use of nanoscale zerovalent iron (nZVI) to remediate contaminated

groundwater has received a great deal of attention in the past decades (Henderson, 2007), due to its potential for broader application and higher reactivity compared to other traditional remediation techniques. The nZVI particles can be used to treat contamination by incorporating the particles in a permeable reactive barrier (Henderson, 2007). Once the barrier is designed and installed, groundwater will flow through the barrier where the contaminated groundwater is treated and clean water will continue its path. Another emerging technology based on nZVI includes injections of nZVI slurry into subsurface and provide high efficient reaction to destroy contaminants in the source zone (Zhang, 2003).

Another application of nanotechnology for remediation is the use of carbon nano-tubes (CNTs). Studies have been conducted to explore the exceptional sorption capabilities of CNTs to remove heavy metals from contaminated waters (Naghizadeh et al., 2012). Current technologies such as coagulation can produce toxic sludge and have low removal rates. The use of CNTs could increase the removal efficiencies and be used in various treatment scenarios. Carbon nano-tubes are graphene layers rolled into cylindrical tubes and can be either multi- or single-walled. Their unique characteristics such as high aspect ratio make them applicable for many applications including remediation. However, the production of CNTs is expensive, preventing extensive research and applications for environmental remediation.

Carbon nano-onions (CNOs) are a new member of the carbon family added in 1992 when they were discovered by Daniel Ugarte (Ugarte, 1993). They receive their name from a cage-in-cage structure, consisting of multi-layered concentric graphene spherical shells, displayed in Figure 1. Carbon nano-onions have high surface area and

when compared to common adsorbents such as granular activated carbon (GAC) are expected to possess a higher sorption capacity. With a recently developed and more efficient synthesis process, these nanoparticles could potentially be extremely useful for sorption of heavy metals in contaminated groundwater and soil. A synthesis process using a laser-assisted combustion process can ensure high quality and fast growth of CNOs in open air (Gao et al., 2011). Chapter 3 of this work explores the production, characterization, and transport of CNOs for the use in remediating heavy metal ions in saturated porous media. The sorption capacity of CNOs in comparison with C_{60} was explored for metal ions including zinc, copper, cadmium, nickel, and lead.

Figure 1. Carbon nano-onion molecular structure (University of Nebraska Lincoln, 2012).

3.0 Transport and Retention of Nanoparticles in Porous Media

As previously discussed, some nanoparticles (e.g. nZVI) may be intentionally injected into subsurface for groundwater remediation purposes. Although nanoparticle applications have great potentials, there are unknown behaviors of these particles once released into the environmental. Hence understanding their fate and transport in the environment is important for remediation design. On the other hand, nanoparticles may enter the environment accidentally due to releases during production, use, or disposal. These nanomaterials may end up in natural water systems and could enter drinking water

sources or agricultural fields. This could create a hazardous situation for human health and the ecosystem.

The fate and transport of nanoparticles in the environment are controlled by many physical and chemical variables, such as solution ionic strength, pH, and surface charge. According to clean-bead filtration theory (CFT) (Yao et al. 1971), particle transport and deposition in porous media can be described as a two-step process, i.e., transport and attachment. The first step, transport to the vicinity of the grain (collector) surface, is a result of three governing mechanisms, i.e., interception, gravitational sedimentation, and diffusion. The transport is typically quantified by the single collector efficiency $\eta 0$ (Tufenkji and Elimelech 2004; Long and Hilpert 2009), which reflects the frequency of particle collisions with the grain surface. The second step, attachment to the grain (collector) surface, is directly related to the interaction energy between the particle and the collector surfaces. The attachment is typically quantified by the collision efficiency factor α, which represents the fraction of the collisions that lead to successful attachment. Currently, no single theory can predict α when the surface charges of the particles and collector are opposite, namely under unfavorable conditions. The Derjaguin-Landau-Verwey-Overbeek (DLVO) theory (Elimelech et al. 1995), which includes the sum of the electrostatic interactions and van der Waals interactions, was used to qualitatively analyze the particle – collector interaction. In general, the results of particle transport experiments often do not agree with the qualitative predictions based on the theory (Elimelech et al. 1995).

Many studies have been conducted to understand the transport of colloid and nano-sized particle transport in porous media (Wang et al., 2012; Lecoanet et al, 2004;

Ben-Moshe et al., 2010). Most of the studies have focused on spherical particles in model porous media such as clean quartz sand or spherical glass beads. In reality, nanoparticles can be found in many shapes such as rod-shape and aggregates may form non-spherical colloids. The differences in the shape could greatly change the predicted transport and retention of these nanoparticles in the subsurface. Therefore more research on the effect of shape on the transport and retention at the nano-scale is warranted. In this work, we stretched spherical polystyrene nanoparticles into various aspect ratios and compared their transport and deposition behaviors in environmentally relevant conditions.

Column studies are traditionally used to gain insights on the retention of particles in the porous media, which, however are unable to make direct observations of the mechanisms governing the transport and often require destruction of the column to measure average particle concentrations. Another more recent approach to gain understanding of particle transport is using micromodels to directly observe attachment at the pore scale. Micromodels involve using manufactured flow cells and the injection of nanoparticles through the cell under a microscope. The main set-backs with this technique are the inability to view attachment over several pore scales and poor resolution.

This study uses a newly developed technique to observe nanoparticle transport and attachment using Laser Scanning Cytometry (LSC). Laser Scanning Cytometers utilize a fluorescent microscope and mobile stage for image analysis over a larger scan area, shown in Figure 2. The main advantages of using LSC are the ability to view the

spatial distribution of particles in porous media, quantifiable data can be obtained, and a large scan area may be used (several centimeters).

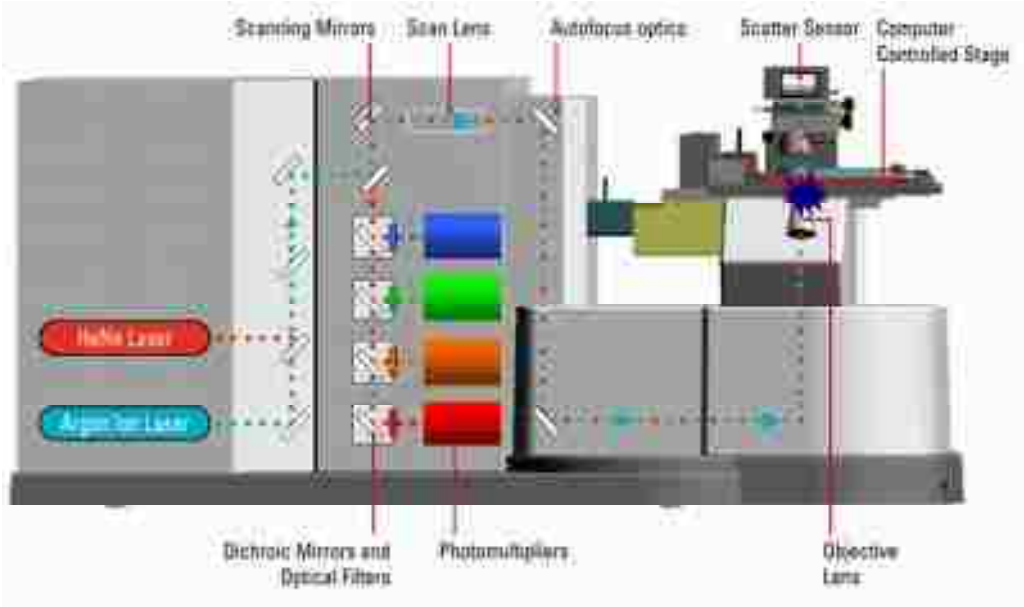

Figure 2. Schematic of Laser Scanning Cytometer. (Adapted from Compucyte, 2011).

References

Ben-Moshe, T., Dror, I., Berkowitz, B., 2010. Transport of metal oxide nanoparticles in saturated porous media. Chemosphere 81 (3), 387-393.

Compucyte, 2011. How LSC technology works. http://www.compucyte.com/howlscworks.htm

Elimelech, M., Gregory, J., Jia, X., Williams, R. A., 1995. Particle deposition and aggregation: measurement, modelling and simulation. Woburn, MA, Butterworth-Heinemann.

Gao, Y., Zhou, Y. S., Park, J. B., Wang, H., He, X. N., Luo, H. F., Jiang, L., Lu, Y. F., 2011. Resonant excitation of precursor molecules in improving the particle

crystallinity, growth rate and optical limiting performance of carbon nano-onions. Nanotechnology 22, 165604.

Henderson, A. D., Demond, A. H., 2007. Long-term performance of zero-valent iron permeable reactive barriers: a critical review. Environ. Eng. Sci. 24 (4), 401-423.

Hickman, K., 2002. Nanomaterials: it's a small, small world. http://www.csa.com/discoveryguides/nano/overview.php.

Lecoanet, H. F., Bottero, J., Wiesner, M. R., 2004. Laboratory assessment of the mobility of nanomaterials in porous media. Environ. Sci. Technol. 38 (19), 5164-5169.

Long, W., Hilpert, M., 2009. A correlation for the collector efficiency of brownian particles in clean-bed filtration in sphere packings by a Lattice-Boltzmann method. Enviro. Sci. Technol. 43 (12), 4419-4424.

Lovgren, S., 2005. Spray-on solar-power cells are true breakthrough. http://news.nationalgeographic.com/news/2005/01/0114_050114_solarplastic.html.

Mann, S., 2006. Nanotechnology and construction. *http://www.nanoforum.org/dateien/temp/Nanotech%20and%20Construction%20Nanoforum%20report.pdf?08112010050156*.

Naghizadeh, A., Yari, A. R., Tashauoei, H. R., Mahdavi, M., Derakhshani, E., Rahimi, R., Bahmani, P., Daraei, H., Ghahremani, E., 2012. Carbon nanotubes technology for removal of arsenic from water. Arch. Hyg. Sci. 1 (1), 6-11.

Nanotechnology Now, 2012. Some examples of how nanotechnology impacts our lives now. http://www.nanotech-now.com/current-uses.htm.

National Nanotechnology Initiative. Size of nanoscale. http://www.nano.gov/ nanotech-101/what/nano-size.

Tufenkji, N., Elimelech, M., 2004. Correlation equation for predicting single-collector efficiency in physicochemical filtration in saturated porous media. Enviro. Sci. Technol. 38 (2), 529-536.

Ugarte, D., 1993. Formation mechanism of quasi-spherical carbon particles induced by electron bombardment. Chem. Phys. Lett. 207 (4-6), 473-479.

Understanding Nanotechnology, 2007. Nanotechnology applications. http://www.understandingnano.com/nanotech-applications.html.

University of Nebraska Lincoln, 2012. Nanoscale carbon onion for remediation. http://www.unl.edu/nanowater/research-topics.

Wang, C., Bobba, A. D., Attinti, R., Shen, C., Lazouskaya, V., Wang, L., Jin, Y., 2012. Retention and transport of silica nanoparticles in saturated porous media: effect of concentration and particle size. Environ. Sci. Technol. 46 (13), 7151-7158.

Yao, K., Habibian, M. T., O'Melia, C. R., 1971. Water and wastewater filtration: concepts and applications. Environ. Sci. Technol. 5 (11), 1105-1112.

Zhang, W., 2003. Nanoscale iron particles for environmental remediation: an overview. Journal of Nanoparticle Research 5, 323-332.

CHAPTER 3

CHARACTERIZATION OF CARBON NANO-ONIONS FOR HEAVY METAL ION REMEDIATON

Abstract

Carbonaceous nanomaterials, such as fullerene C_{60}, carbon nanotubes, and their functionalized derivatives have been demonstrated to possess high sorption capacity for organic and heavy metal contaminants, indicating a potential for remediation application. The actual application of these nanomaterials, however, is often hindered by the high cost of materials and the limited understanding of their mobility in porous media. In this work, carbon nano-onions (CNOs), a relatively new addition to the carbonaceous nanomaterials, were synthesized in a cost-effective way using a laser-assisted combustion synthesis process, and carefully characterized for their potential remediation application. Surface oxidized CNOs possessed 10 times higher sorption capacity than C_{60} for heavy metal ion contaminants including Pb^{2+}, Cu^{2+}, Cd^{2+}, Ni^{2+}, and Zn^{2+}. CNOs aqueous suspension can be very stable in NaCl solution at ionic strength up to 30 mM and $CaCl_2$ solution at ionic strength up to 4 mM $CaCl_2$ when pH ranged from 5 to 9, which are consistent with environmentally relevant conditions. Interactions of CNOs with iron oxide and silica surfaces under favorable condition were found to be electrostatic in origin. Mobility of CNOs in quartz sands was controlled by electrolyte type and concentration. Approximately 4.4, 25.1, and 92.5 % of injected CNO mass were retained in the sand column in ultrapure water, 1 mM NaCl, and 1 mM $CaCl_2$ solutions, respectively.

1.0 Introduction

The US Environmental Protection Agency (EPA) (2004) estimated that there are 294,000 hazardous waste sites in the US, which may require $373 billion to $1,694 trillion dollars to clean up (Burroughs 2000). While different remediation technologies have been developed in recent years, nanotechnology holds promise to provide solutions with improved efficiency and performance. Carbonaceous nanomaterials, such as fullerene C_{60} and carbon nanotube (CNT), and their functionalized derivatives have been demonstrated to possess high sorption capacity. For example, C_{60} fullerene was found to be able to adsorb large amount of organic contaminants (Yang et al. 2006). CNT, after surface modification, has very high sorption capacity for heavy metals (Li et al. 2003; Mauter and Elimelech 2008). Comparing with traditional sorbents, carbonaceous nanosorbents showed rapid equilibrium rates, high sorption capacity and effectiveness over a broad pH range, due to their high surface area to volume ratio, controlled pore size distribution, and manipulatable surface chemistry (Mauter and Elimelech 2008). While these materials possess the potential for remediation application, two major challenges need to be explored before actual application, including: (1) the cost of materials and (2) the mobility of material in porous media.

Unfortunately, both C_{60} and CNT are extremely expensive, preventing extensive research, and applications for environmental remediation. Carbon nano-onions (CNOs) were added as a new member of the carbon family tree when they were discovered by Daniel Ugarte in 1992 (Ugarte 1993). CNOs, also called onion-like fullerenes and buckyonions, have a cage-in-cage structure, consisting of multi-layered concentric graphene spherical shells. Previously, CNOs were produced by high-energy electron

irradiation of carbonaceous materials, thermal treatment of fullerene black, and dc arc discharge. These methods can only produce a small quantity of CNOs with a mass of by-products, which are very difficult to separate (Chen et al. 2001). Recently, we developed a laser-assisted combustion synthesis process for fast growing of high quality CNOs in the open air (Gao et al. 2011). Utilizing 25 torches in a straight line and optimizing the use of laser output energy, a mass production rate of 500 g/h can be achieved in the lab, with estimated cost much lower than C_{60} and CNT. While additional efforts will be needed to further commercialize the CNO production for treating contaminated soil and groundwater, the potential of large scale production is certain.

Cost-effective production of CNOs improves their feasibility for remediation application. When compared to common adsorbents such as coconut coir, granular activated carbon (GAC), and crab shell powder, which already can be synthesized in large scale, CNOs are expected to possess higher sorption capacity and faster equilibrium rate as reported for other carbonaceous nanosorbents (Mauter and Elimelech 2008). Currently, however, no data is available to directly support the possibility of using CNOs for heavy metal ion remediation. Thus, a detailed characterization on CNOs particularly for environmental remediation becomes necessary. Specifically, it is important to compare and contrast the sorption capacity of CNOs with that of better studied carbonaceous nanomaterials such as C_{60} and CNTs. In addition, it is critical to investigate the mobility of such material once injected into subsurface porous media for potential in situ remediation practice.

In this work, we conducted comprehensive characterization on CNO powder synthesized in our lab by conducting X-Ray diffraction (XRD) analysis, surface area

measurement, and Raman Spectroscopic analysis. Sorption experiments were conducted on surface oxidized CNOs to compare their sorption capacity with C_{60}. We developed a procedure to produce CNO suspension that can be very stable at environmentally relevant levels of pH, electrolyte types, and ionic strengths. CNO particle size distribution and zeta potentials in the solution were carefully characterized. Interactions of CNOs with iron oxide and silica surfaces, important components of aquifer porous media, under favorable condition, were evaluated using a quartz crystal microbalance with dissipation (QCM-D) monitoring system. Column experiments were conducted to evaluate the mobility of CNOs in silica sand.

2.0 Materials and Methods

2.1 Synthesis of carbon nano-onion

A highly efficient and scalable combustion process developed recently by Gao et al. (2011) was employed to grow CNOs in open air. This method used laser irradiation to achieve resonant excitation of precursor molecules. The flames were generated using a welding torch with a 1.5 mm orifice tip. The precursors were a mixture of ethylene (C_2H_4) and oxygen (O_2) with a gas flow ratio of 5:3. A wavelength-tunable CO_2 laser (PRC, spectral range from 9.2 to 10.9 μm) was used. The laser beam at a wavelength of 10.532 μm was used to resonantly excite the wagging mode ($\nu 7$, 949.3 cm^{-1}) of the ethylene molecules to achieve effective energy coupling. The laser beam was directed right above the top of the nozzle and perpendicularly to the flame axis. The laser beam was focused using a ZnSe convex lens (focal length = 254 mm) to 2 mm in diameter. Silicon wafers with dimensions of 5 x 5 x 0.6 mm^3 were placed on top of the flames to collect CNOs. This method is able to produce highly concentric CNO particles, with a

diameter of ca. 5 nm. Figure 1 provides a transmission electron microscopy (TEM) image of produced CNOs.

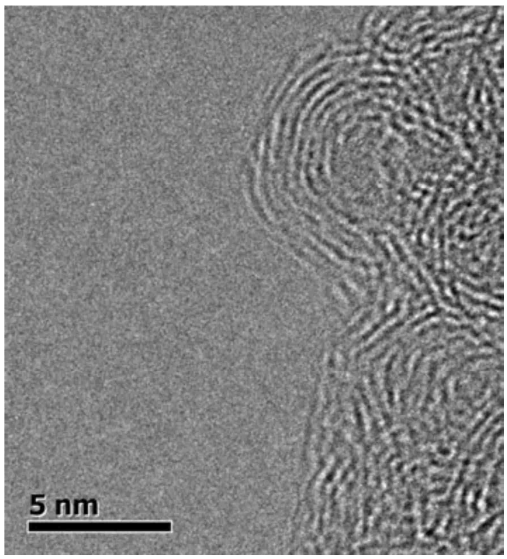

Figure 1. TEM image of CNOs

2.2 X-Ray diffraction

XRD analysis of CNO powder was conducted using a Ringaku Miniflex X-Ray diffractometer (Rigaku Corporation, Tokyo 196-8666, Japan) operated at 30 kV and 15 mA, with a scan speed of 0.5 deg/min. For comparison purposes, XRD analysis was also conducted for C_{60} fullerene (99.9 % MER Corporation Tucson, AZ).

2.3 Surface area measurement

Surface area of CNO powder and purchased C_{60} particles were measured using a NOVA 4200 Multi-station Gas Sorption Analyzer (Quantachrome Instruments, Boynton Beach, FL). About 20 mg of sample was put into a 6-mm diameter sample cell, followed by 2 hours of degassing process at 150 ˚C. The measurement was based on nitrogen gas adsorption, and multipoint BET method was used to calculate the surface area.

2.4 Raman spectroscopic analysis

Raman spectroscopy measurements were taken with three different laser excitation wavelengths of 532, 633, and 785 nm using a Senterra Raman microscope (Bruker Optics Inc.), covering spectral range of 20 to 4,500 cm^{-1}.

2.5 Surface oxidation

In order to investigate the sorption capacity of CNOs for heavy metal contaminants, a surface oxidation process was first applied to introduce carboxylate groups onto the CNO surface using either HNO_3 or NaOCl. Parallel oxidation was applied to C_{60} for comparison purposes by modifying a procedure developed in Wu (2007). In brief, 100 mg CNOs or C_{60} was first heated in an oven at 300 ˚C for 30 min., and then immersed in 65 % HNO_3 in an ultrasonic bath for 30 min., stirred continuously for 36 h at 25 ˚C. It was then repeatedly washed using DI water and centrifuged to separate liquid, until the solution pH reached 5. The final product was dried at 70 ˚C for 12 h. Modification using 6 % NaOCl used a similar procedure as HNO_3, except that the solution was heated to 85 ˚C for 6 h while stirred.

2.6 Sorption experiments

Sorption capacity of surface oxidized CNOs and C_{60} for metal ion contaminants, including Zn^{2+}, Cu^{2+}, Cd^{2+}, Ni^{2+}, and Pb^{2+}, was investigated. In brief, 35 mL of a 2 mg/L heavy metal ion solution in deionized water was mixed with 10 mg of nanomaterials for 48 h. The pH of the solution was adjusted to 7.0 using NaOH and HCl solutions. After 30 min of centrifuging at 3,000 rpm, the suspension was filtered through a 0.22 μm membrane. The heavy metal ion concentrations before and after exposing to the nanomaterials were measured. Duplicate tests were conducted for all the sorption experiments. The goal of sorption experiments at this stage is to provide the first piece of

information on the capacity of CNOs for heavy metal sorption; thus, experimental parameters were limited to fixed solid/liquid ratio, contact time, and pH.

2.7 Stable CNO aqueous suspension development

An organic solvent exchange method (Wang et al. 2008) was modified to prepare stable CNO aqueous suspension. First, 10 mg of CNO powder was dissolved in 20 mL HPLC-grade toluene by stirring the mixture on a stir plate at 500 rpm for 6 h, resulting in a dark mixture. The mixture was gently introduced into a beaker containing 900 mL of ultrapure water, forming two distinct phases. The resulting solution was sonicated in a sonicating bath (Branson 3510RDTH sonicator, 100 W, 42 kHz, Danbury, CT) in a fume hood for 8 h for complete evaporation of toluene. Deionized water was added to the mixture throughout the sonication process to account for evaporation of water. The final solution was moved to a 1 L flask and filled with deionized water to the 1 L mark to produce a 10 mg/L concentration.

2.8 Diffuse reflectance infrared fourier transform spectroscopy (DRIFTS)

DRIFTS measurements (Vertex 70 FTIR, Bruker Optics Inc.) were taken for pristine CNO powder and CNO recovered from a stable liquid suspension to investigate the potential modifications on CNO surface during suspension development. Approximately 1 L of the prepared CNO suspension was centrifuged and left to air dry for 48 h. Resulting CNO solid was used for DRIFTS measurements.

2.9 Particle size distribution and zeta potential measurement

The electrophoretic mobility of the CNO in aqueous suspensions with varied ionic strength and pH values was obtained using a ZetaSizer Nano-ZS ZEN3600 (Malvern

Instruments, Scarborough, MA, USA). Experimentally determined electrophoretic mobility values were converted to zeta potentials for each condition using the Smoluchowski equation (Sze et al. 2003). The average hydrodynamic diameters of the CNO aggregates and the particle size distribution in the aqueous suspensions of various ionic strength and pH was obtained using dynamic light scattering (DLS) (ZetaSizer Nano-ZS ZEN3600 Malvern Instruments, Scarborough, MA, USA).

2.10 Scanning electron microscopy (SEM)/energy dispersive X-ray (EDX)

Microscopic pictures of CNO aqueous suspension were obtained using a LEOL JSM-6360 SEM. CNO nanoparticles were deposited onto a carbon planchet surface by leaving a drop of CNO suspension to dry overnight. The SEM images were taken with a working distance of 10 mm. An EDX system (INCA, oxford instruments) was connected to analyze the elemental information on the representative CNO particles identified by SEM.

2.11 UV–Vis spectroscopy

The UV–Vis spectrum of CNO suspension was recorded using a UV–VIS–NIR Scanning Spectrophotometer (Shimadzu Corporation, MD). A distinct peak was identified at a wavelength of 248 nm for a CNO aqueous suspension of 10 ppm. The UV–Vis analysis was then applied for CNO suspension that was diluted 2, 5, 10, 25, 50, and 100 times. The response 248 nm was found linearly correlated to CNO concentration with an R-square of 0.9983. The correlation was later used in the column experiments to determine aqueous CNO concentration.

2.12 QCM-D experiments

A QCM-D E-1 unit (Q-Sense AB, Sweden) was used to measure the deposition of CNO onto a silicon dioxide-coated surface (QSX 303, Q-Sense) and an iron oxide-coated surface (QSX 326, Q-Sense). The QCM-D E-1 unit is composed of a thin quartz disk placed on a pair of electrodes, where a voltage is applied. A flow chamber directs the solution to flow parallel across the sensor surface with the use of a peristaltic pump. As deposition of CNO occurs, an increase in the mass of the crystal causes a shift in the resonance and overtone frequencies. The mass of CNOs deposited onto the crystal can be determined with use of the Sauerbrey relationship (Quevedo and Tufenkji 2009). The change in the frequency over a time period of 30–60 min was evaluated to determine the deposition rate of the nanoparticles onto the crystal surface based on Equation 1.

$$r_d = \frac{d\Delta f_3}{dt} \quad (1)$$

In Equation 1, r_d is the CNO deposition rate, $d\Delta f_3$ is the shift in third resonance or overtone frequency, and dt is the time period examined (Quevedo and Tufenkji 2009).

Prior to each experiment, the tubing and measurement chamber were flushed with 2 % sodium dodecyl sulfate (SDS), followed by a sufficient flush of DI water. The crystals were also cleaned prior to each experiment according to the cleaning protocol suggested in the user's manual, rinsed with deionized water, and dried with nitrogen gas. In order to ensure adequate cleaning, QCM-D experiments were repeated after cleaning of the sensor. A background solution containing the electrolyte of interest and desired pH was flowed through the chamber at 0.100 mL/min (± 0.002 mL/min), which was maintained at a constant temperature of 22 ˚C, until the frequency of the third overtone

stabilized (drift < 0.5 Hz for 10 min). The CNO suspension was then introduced at the same flow rate.

At the studied solution conditions (i.e., pH values of 5, 7, and 9), both the silica surface and CNOs are negatively charged, very little deposition would occur on a pure silica surface. The sensor was thus modified using positively charged poly-L-lysine (PLL) polyelectrolyte to induce a favorable deposition condition, a similar approach was used for several previous studies (Chen and Elimelech 2006, 2008). The PLL solution consisted of 10 mM N-(2-hydroxyethyl) piperazine-N0-(2-ethanesulfonic acid) (HEPES, H4034-100G, Sigma–Aldrich, St. Louis, MO) and 100 mM NaCl. A 0.1 g/L PLL solution was flowed through the chamber until a stable baseline was achieved, resulting in a frequency shift of about 7 Hz. A stabilized baseline indicates the surface was fully saturated and no more attachment on the silica surface could occur. After stabilization, HEPES solution was then flowed through the module to rinse the PLL layer, followed by the flow of electrolytes of interest without nanoparticles. Finally, the CNO suspension in the electrolyte of interest was flowed across the sensor for approximately 60 min to achieve an initial deposition rate for analysis. The frequency shift was measured and the initial deposition rate was determined with the change in frequency of the third overtone over the tested time.

2.13 Column experiments

Column experiments were conducted to evaluate the transport of CNO through porous media under a range of environmentally related conditions. A borosilicate glass column (2.5 cm dia x 15 cm length) was packed with 30–50 mesh Ottawa sand (US Silica, Berkeley Springs, WV). The column endplates were fitted with two 40-mesh

nylon screens and a 40 μm nylon filter to support the solid phase and promote uniform flow. Following packing, the columns were flushed with CO_2 gas for 20 min to facilitate subsequent dissolution of entrapped gas during the water imbibition process. About 10 pore volumes of de-aired water containing a background electrolyte were then introduced into the column in an upflow mode. Following complete water saturation, a nonreactive tracer test (NaBr) was performed for each column to assess flow characteristics, confirm the pore volume, and measure hydrodynamic dispersion. A pulse injection (c.a., 4 pore volumes) of CNO suspension was then applied to the column using a syringe pump (Harvard Apparatus, Holliston,MA) at a nominal flow rate of 1.0 mL/min. Effluent samples were collected continuously using an ISCO Retriever II fraction collector. Effluent solution was scanned using UV–Vis spectrophotometer, and CNO concentration was calculated using the correlation between the UV absorbance at 248 nm and CNO concentration developed previously.

3.0 Results and Discussion

3.1 Pristine CNO powders

The XRD analysis of CNO powders are shown in Figure 2. Instead of a typical diffraction peak at about 26˚ corresponding to graphite, we observed one major peak at 30.7˚ with counts of 585 and a moderate peak at about 55˚. The peak is relatively wide, indicating that the structures in the product are not as highly crystallized as in C_{60}. Measured BET surface areas are in the range of 79.5–84.6 m^2/g for CNOs, which is comparable to the reported surface area of multi-walled CNT of 94.7 m^2/g (Yang et al. 2006).

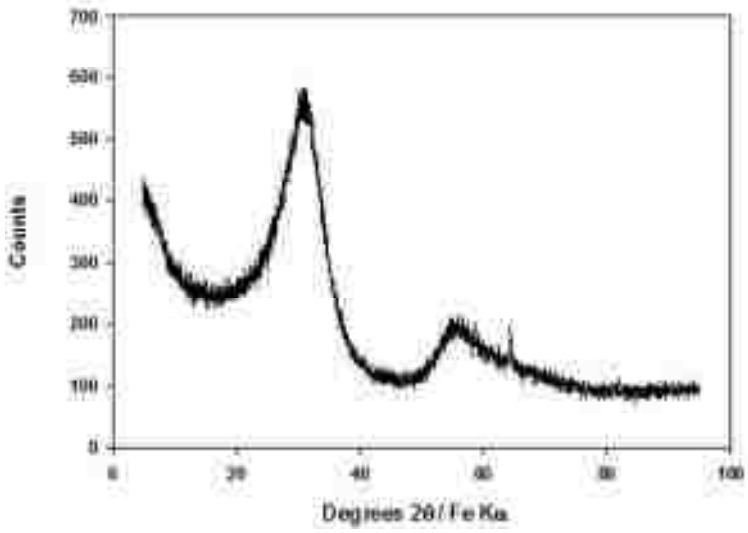

Figure 2. XRD pattern of CNO.

Figure 3 provides the Raman spectra of CNOs at various wavelengths. No obvious Raman shifts were identified with the laser excitations of 633 and 785 nm. Two dominant Raman shifts at 1330.8 and 1592.13 cm^{-1} were observed with an excitation of 532 nm, which is consistent with multiple reports on CNO Raman spectra (Roy et al. 2003; Plonska-Brzezinska et al. 2011;Gao et al. 2011; Katumba et al. 2008). In a previous study, the two bands were fitted into five different bands, one of which was ascribed to the amorphous carbon (Gao et al. 2011).

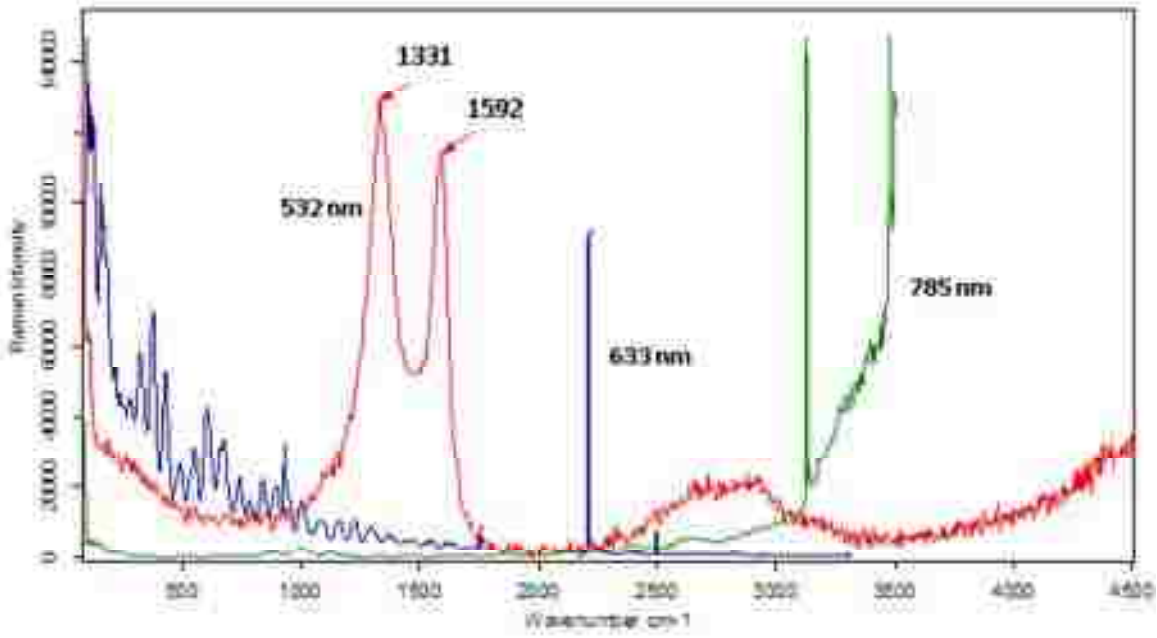

Figure 3. Raman spectra of CNOs at various excitations of 532, 633, and 785 nm.

3.2 Sorption capacity of oxidized CNOs

Equilibrium sorption experiments were performed to test the sorption capacity of the modified CNOs and C_{60} (oxidized in the same way for comparison) for Zn^{2+}, Cu^{2+}, Cd^{2+}, Ni^{2+}, and Pb^{2+}. Oxidation of CNO, using NaOCl or HNO_3, may introduce various oxygen containing functional groups onto CNO surfaces, therefore, improving surface hydrophilicity and also increasing available sorption sites (Chen et al. 2009; Wu 2007; Yang et al. 2006). The modification process can be described as (Wu 2007).

$$10C_n + 6H^+ + 6NO_3^- + 2H_2O \rightarrow 10C_{n-1} - COOH + 3N_2 \quad (1)$$

$$2C_n + 3OCl^- + 2H_2O \rightarrow 2C_{n-1} - COOH + 3Cl^- \quad (2)$$

As illustrated in Figure 4, CNO showed stronger sorption capacity comparing with C_{60} for both NaOCl and HNO_3 modification. NaOCl-modified CNOs seemed to

have higher sorption capacity for Zn^{2+}, Cd^{2+}, and Ni^{2+} than HNO_3-modified CNOs, which may be due to higher oxidizing ability of NaOCl than that of HNO_3. No significant difference was observed for Cu^{2+} and Pb^{2+}. NaOCl-modified CNOs possessed a relatively constant sorption capacity of ca. 6 mg/g for all of the five metals tested, more than 10 times higher than that of the functionalized C_{60} fullerene for Zn^{2+}, Cd^{2+}, Ni^{2+}, and at least equivalent to that of the functionalized C_{60} for Cu^{2+} and Pb^{2+}. The significantly higher sorption capacity of CNOs could be attributed to the structural differences between CNO and C_{60}.

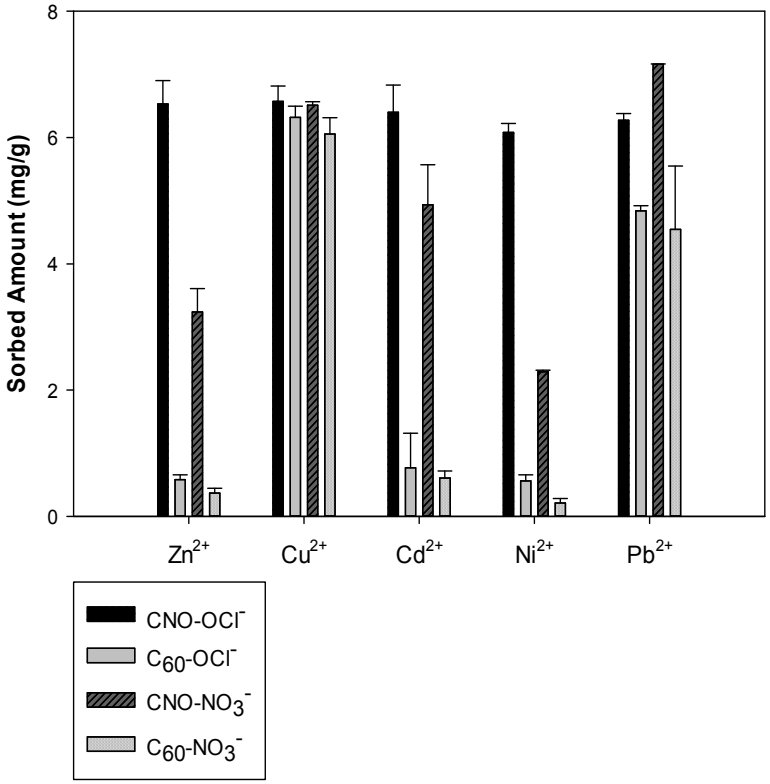

Figure 4. Comparison of sorption capacity of NaOCl-modified and HNO_3-modified CNO and C_{60} nanomaterials for Zn^{2+}, Cu^{2+}, Cd^{2+}, Ni^{2+}, and Pb^{2+} (sorbent mass/liquid = 10 mg/35 mL).

Oxidation process essentially would create some defects on the surfaces, where –COOH groups may locate (Wu 2007). XRD results (Fig. 2) revealed that the structures in the CNOs are not as highly crystallized as in C_{60}. Thus, oxidized CNOs might have more –COOH groups on its surface than oxidized C_{60}, leading to observed higher sorption capacity.

It was reported (Li et al. 2003) that the sorption capacity of functionalized CNTs for Cd^{2+} is about 6.5 mg/g under the similar sorbent mass/liquid ratio (i.e., 10 mg/35 mL). It is anticipated that higher sorption capacity of our CNO will be achieved if we increase the sorbent mass/liquid ratio, as previously reported for CNT sorption of metal contaminants (Wu 2007). Oxidation using 6 % NaOCl solution, commonly known as bleach and frequently used as a disinfectant or a bleaching agent, is a very cost effective and feasible approach. Functionalized CNOs possess a higher (or at least equivalent) sorption capacity than (as) commercially available carbonaceous nanomaterials, including C_{60} and CNT, for heavy metal contaminant sorption. CNO, however, is 100 times more cost effective than C_{60} and CNT, which makes it feasible for remediation applications.

3.3 CNO suspension

Similar to C_{60} (Wang et al. 2008), CNO nanoparticles can form stable aggregates in the liquid suspension. As shown in the representative SEM image (Fig. 5), these aggregates are irregularly shaped, with 4–5 angular protrusions. The longest dimension is about 200 nm, and the shortest dimension is about 50–100 nm. The aggregates do not show any crystalline property, as opposed to the reported nanocrystal structure for C_{60} aggregates (Fortner et al. 2005; Chen and Elimelech 2006).

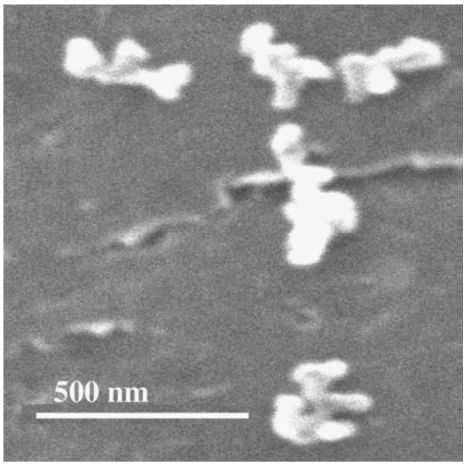

Figure 5. SEM image of CNO nanoparticle aggregation.

EDX analyses (Figure 6) were conducted on six different locations where CNO aggregates were deposited. Carbon and oxygen were the only two major elements in all six locations. Carbon weight percentage varied from 94.8 to 98.15 %, and oxygen weight percentage varied from 1.85 to 4.81 %. A trace amount of sodium, with weight percentage varied from 0.26 to 0.39 %, was identified in three out of six measured locations. The amount of sodium element is lower than the detection limit of EXD for sodium (1 %), and the source is not very clear. While carbon is the dominant element for CNO, as expected, the small amount of oxygen may be introduced during the open air synthesis and extended sonication process.

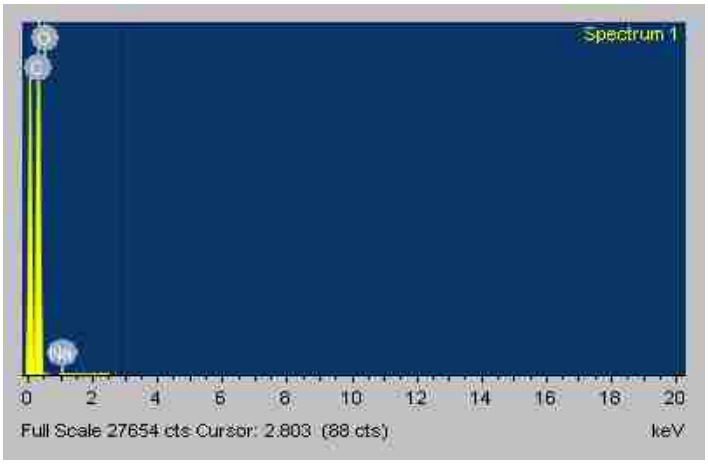

Figure 6. EDX analysis of CNO aggregates dried on a carbon planchet.

The DRIFTS technique was used to investigate the potential modification of the CNO surface during suspension development process. As shown in Figure 7, the spectra for pristine CNOs and CNOs harvested from suspension share several peaks at 3,436–3,450; 2,331–2,367; and 1,634–1,636 cm^{-1}. These peaks appear to be characteristic of CNOs and possibly adsorbed water. Additional peaks at 2,924; 2,854; and 1,385 cm^{-1} for CNOs that went through dispersion and sonication in toluene are probably attributable to the minute amounts of residual toluene in the sample (Figure 7a).

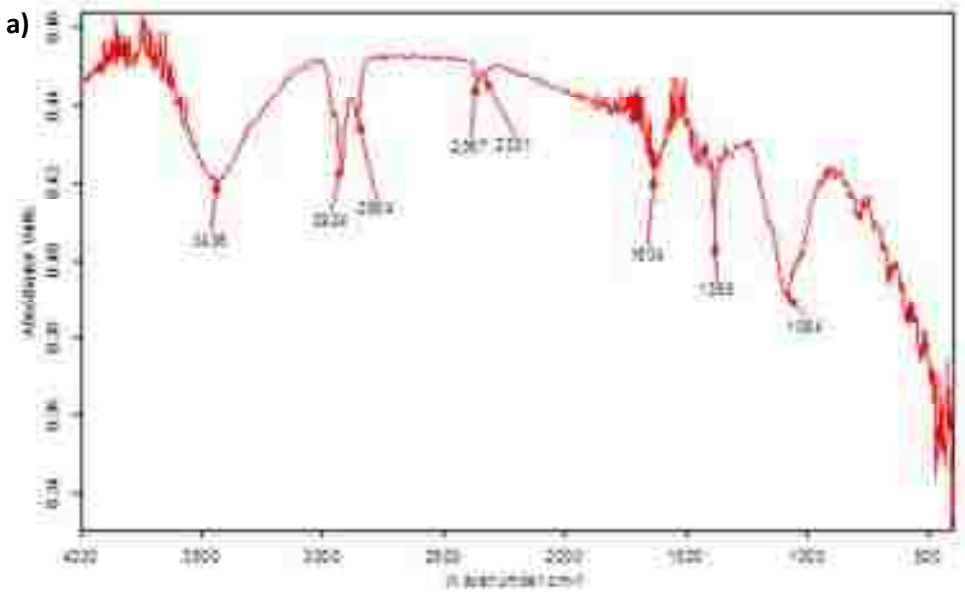

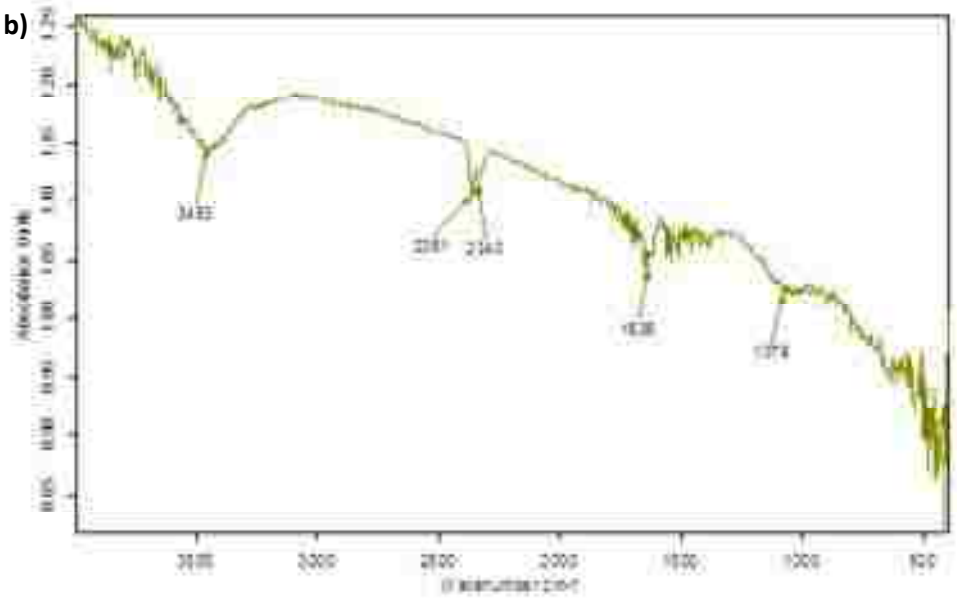

Figure 7. DRIFTS spectra of a) CNO recovered from suspension and b) pristine CNO powder.

3.4 Particle size distribution and zeta potential

As revealed by SEM imaging, CNO aggregates are not spherical in shape. Thus, DLS measurement, which assumes spherical particles, can only provide the size of an equivalent sphere that has the same translational diffusion coefficient as the particle. We believe that such information is also valuable to understand the CNO aggregate properties. Figure 8 shows an example CNO aggregates equivalent diameter distribution in ultrapure water with pH 6.5. In this example, 81.6 % of particles have a hydrodynamic diameter between 122.4 and 295.3 nm, with an average of 187.4 nm.

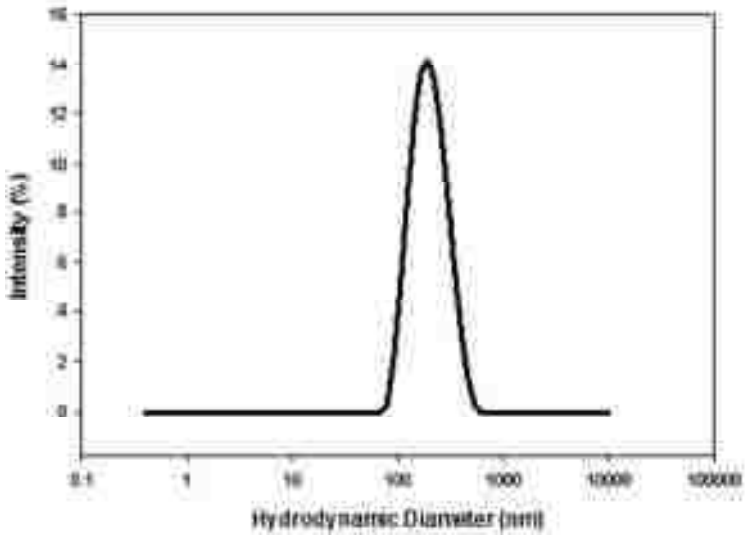

Figure 8. An example CNO aggregates particle size analysis by DLS.

We observed that formation of CNO aggregates can be affected by sonicating processes. A higher power sonicator (Branson 3510R-DTH sonicator, 100 W, 42 kHz, Danbury, CT) produced an average hydrodynamic diameter of 137 nm as measured by DLS in ultrapure water. Meanwhile, an average hydrodynamic diameter of 184.7 nm was produced under exactly same condition, except using a relatively lower power sonicator (Fisher Scientific FS60). Dependence of aggregate diameter on the mixing rate was also reported for C_{60} aggregates formation (Fortner et al. 2005), consistent with our observation. Both suspensions have very similar zeta potential value of ca. -50 mV, indicating similar surface properties.

Effects of pH on zeta potential and particle size were investigated using CNO suspension that has a mean hydrodynamic diameter of 184.7 nm in ultrapure water. As illustrated in Fig. 9, the average particle size kept constant at about 190 nm in the pH range of 3–12. The mean particle size dramatically increases when pH value is smaller than 3, which indicates that CNO suspension tends to become unstable and form large

aggregates when pH is lower than 3. CNO aggregate zeta potential kept as negative, increasing from ca. -59 mV to ca. -3 mV when pH decreases from 11.6 to 1.2. The rate of zeta potential increase had an obvious increase at close to pH 4, also indicating unstable CNO suspension close to this condition, consistent with particle size measurement.

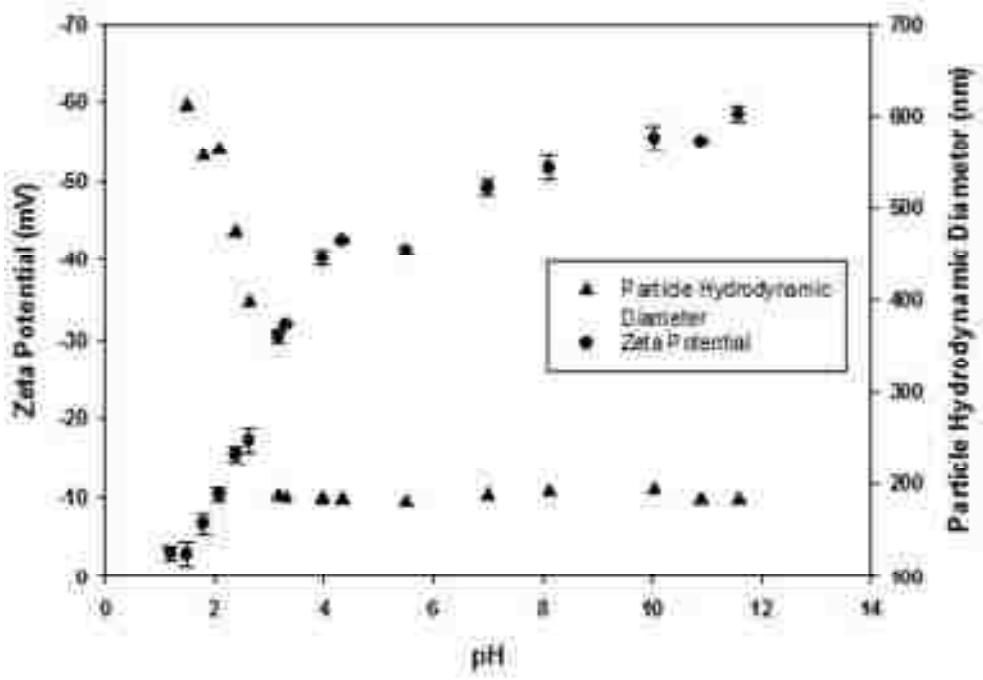

Figure 9. Effects of solution pH on CNO aggregates on zeta potential and mean particle hydrodynamic diameter.

Effects of electrolytes type and ionic strength were investigated under pH 5, 7, and 9 using CNO suspension that has a mean hydrodynamic diameter of 137 nm in ultrapure water. The zeta potential was determined to be negative over the entire range of ionic strengths and all pH values examined. In general, as the ionic strength increases, the particles become less negatively charged as a result of compressing the diffuse double layer of ions at the surface of the particle. The zeta potential ranges from approximately -44 to -18 mV with increasing ionic strength of NaCl and from approximately -30 to -11 mV with increasing ionic strength of $CaCl_2$. The divalent ion (Ca^{2+}) displayed to have a

greater impact on the change in zeta potential compared to the monovalent ion (Na^+), which may be indicative of specific adsorption of Ca^{2+} onto CNO surfaces, similar to a previous study on C_{60} (Chen and Elimelech 2006). The zeta potential seemed to be slightly less negative at pH value of 5.

For all the pH values evaluated here, the average hydrodynamic diameter of the particles seems to remain relatively stable at ca.137 nm at low ionic strengths, 1–10 mM NaCl and 0.1–1 mM $CaCl_2$, shown in Figs. 10 and 11, respectively. At greater ionic strength, 30–300 mM NaCl and 4–100 mM $CaCl_2$, particle aggregation becomes apparent with increasing average hydrodynamic diameter measured. The average particle size showed a greater deviation at higher concentrations of NaCl at pH 5. The stability of CNO aggregates in ionic liquid media is consistent with some reports for semiconductor nanoparticles (e.g., Rodriguez-Cabo et al. 2012).

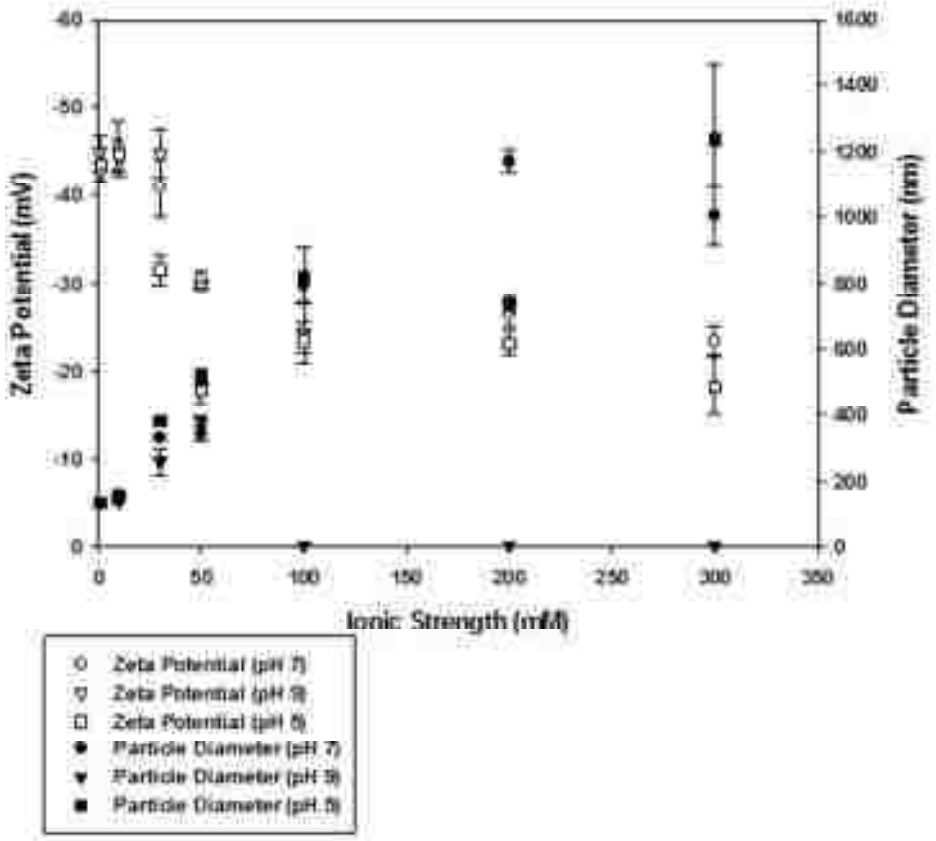

Figure 10. Effects of ionic strength of NaCl on CNO aggregates zeta potential and average hydrodynamic diameter.

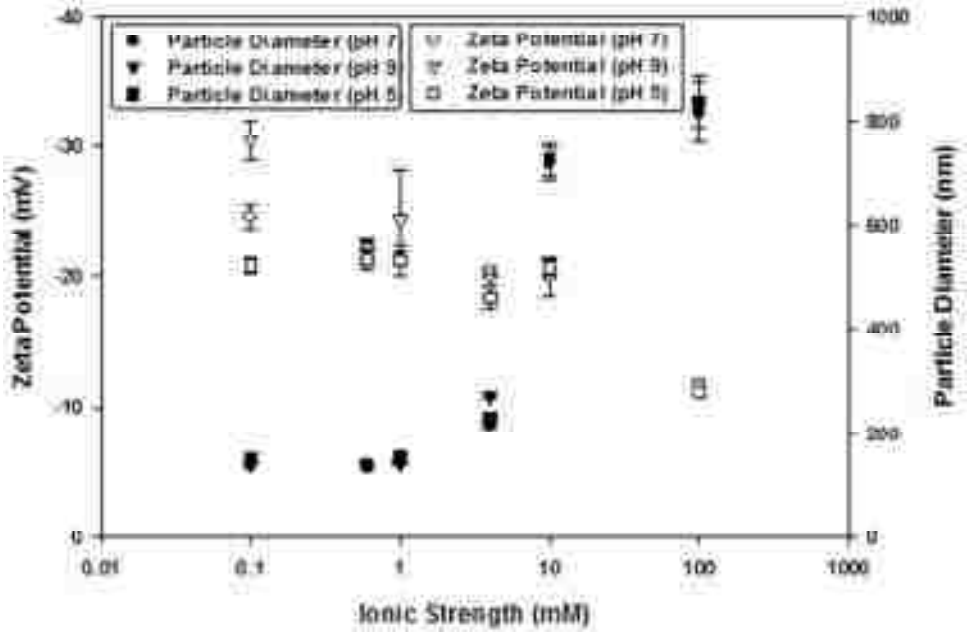

Figure 11. Effects of ionic strength of $CaCl_2$ on CNO aggregates zeta potential and average hydrodynamic diameter.

3.5 CNO deposition under favorable condition

QCM-D experiments were conducted with NaCl solution at ionic strength of 1–30 and 0.1–4 mM $CaCl_2$ at a pH of 7 where the CNO aggregates are relatively stable. We observed a decrease in the deposition rate as the ionic strength increased. The trend for the deposition rate onto PLL-coated silica and iron oxide as functions of increasing ionic strength of NaCl and $CaCl_2$ is shown in Fig. 12. Such an observation is consistent with the Derjaguin–Landau–Verwey–Overbeek (DLVO) theory of colloidal stability. According to DLVO theory, when negatively charged CNO particles approach positively charged PLL-coated silica or iron oxide surfaces at short distances, they are subjected to attractive electric double layer (EDL) and attractive van der Waals (VDW) interaction forces (Elimelech 1991, 1994). As the ionic strength increases, the range and magnitude of attractive double layer interactions will decrease, and leads to reduced CNO deposition

rate. A faster decrease in deposition rate was observed in the presence of Ca^{2+} compared to that of Na^{+}.

The deposition onto the silica surface is more predominant compared to the iron oxide sensor, which can be correlated to the surface charge of the sensors. Although the silica surface was originally negatively charged, coating with PLL makes it positively charged, so that only attractive interactions exist between CNOs and silica surfaces. In such a favorable situation, every collision between CNO particles and silica surface will lead to stable attachment, i.e., collision efficiency factor equals to 1 (Yao et al. 1971). While the iron oxide surface is generally positively charged under solution conditions tested, surface charge heterogeneity may exist for such a material surface, so that the deposition onto the iron-oxide sensor surface did not have as large of a deposition rate. Also, the isoelectric point for iron oxide is near a neutral pH, therefore, the positive surface charge of the iron-oxide sensor would not be as significant at pH 7 used for QCM-D experiments compared to the favorable conditions created with the PLL coating on the silica sensor.

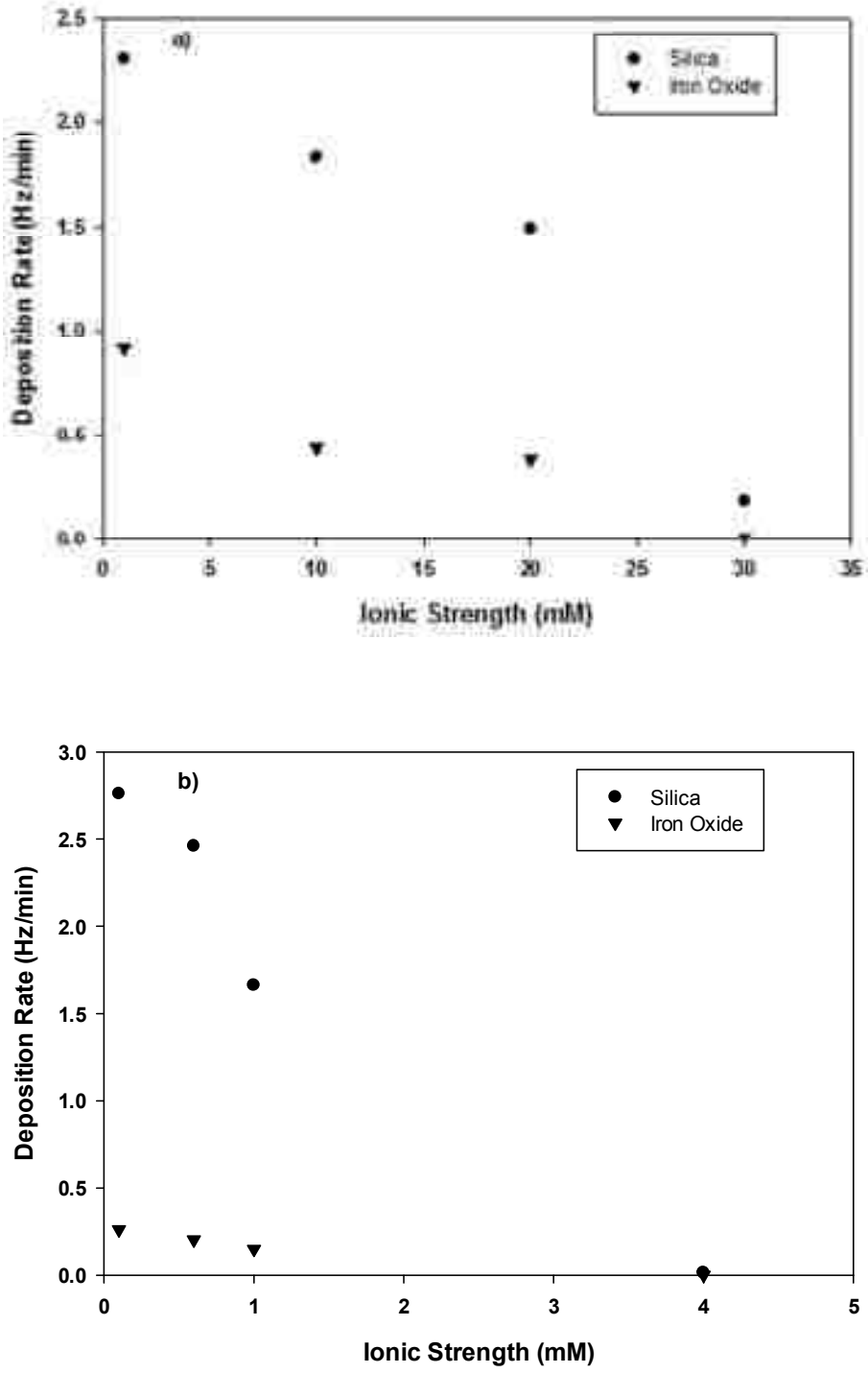

Figure 12. Deposition rate of CNOs onto iron oxide and PLL-coated silica sensor over an increasing ionic strength of a) NaCl and b) $CaCl_2$.

3.6 CNO transport in quartz sand

Transport of CNO suspension in columns packed with quartz sand was evaluated with varied background solution chemistry, including ultrapure water, 1 mM NaCl solution, and 1 mM $CaCl_2$ solution. The breakthrough curves, where relative concentration (C/C0) is plotted against the number of pore volumes (PV) of solution introduced, are presented in Figure 13. For comparison purposes, a tracer breakthrough curve is also plotted.

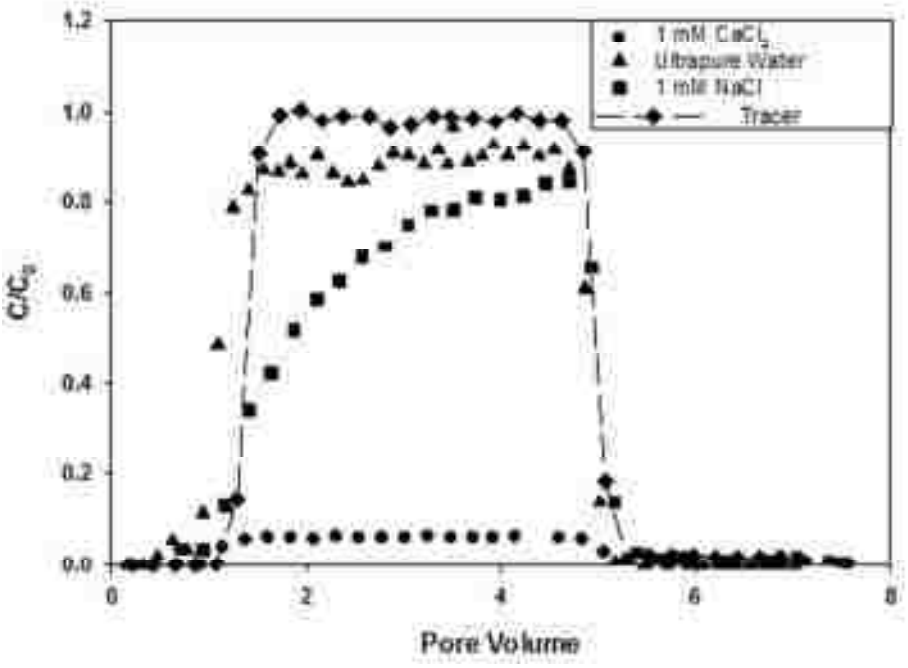

Figure 13. Effluent concentration after pulse injections of CNO suspensions in columns packed with unwashed 30-50 Ottawa sand with ultrapure water, 1 mM $CaCl_2$, and 1 mM NaCl as background solution.

In general, CNO particles were detected in the effluents around 1 PV, slightly earlier than tracer breakthrough. The early breakthrough of CNO particles can be attributed to ‘‘size exclusion’’ effects, where particles cannot access to very fine pores in the column. Very few CNOs were attached on sand when introducing with ultrapure

water, reaching a C/C0 plateau of about 0.91. In contrast, CNO aggregates in 1 mM $CaCl_2$ showed very little breakthrough, with a C/C0 plateau of only ca. 0.06. The breakthrough curve in 1 mM NaCl solution is asymmetric, with an initial gradual rise and a sharp decrease, similar to C_{60} aggregate breakthrough curve reported in Wang et al. (2008). The highest C/C0 reached is 0.84. Mass balance calculation showed that about 4.4, 25.1, and 92.5 % of injected CNO mass were retained in the sand column in ultrapure water, 1 mM NaCl, and 1 mM $CaCl_2$ solutions, respectively.

The retention of CNOs in different solution chemistry seems dominated by the electrostatic double layer repulsion between CNOs and sand surface as predicted by the DLVO theory. Under the evaluated solution chemistry, both sand and CNO surfaces possess negative zeta potential. Measured zeta potentials for CNO aggregates were ca.-46.1 ± 0.2, -45.1 ± 0.3, and -19.1 ± 0.6 mV for ultrapure water, 1 mM NaCl, and 1 mM $CaCl_2$ solutions, respectively. Although not in exactly same conditions, multiple reports (Chen et al. 2011; Kaya and Yukselen 2005) have suggested that sand surface zeta potentials became less negative when ionic strength increased or with the presence of divalent cations. According to the DLVO theory, less negative zeta potentials in $CaCl_2$ solution on both CNOs and sand surfaces will produce lower repulsive energy barrier, leading to more attachment. Higher mobility of CNOs in ultrapure water may also be due to much more negative surface potential of sand in ultrapure water (Chen et al. 2011). The slight retention, ca. 4.4 %, may be attributed to surface charge heterogeneity of sand surface. The sand used in this study was composed mainly of SiO_2, but a small amount of metal oxide impurity may exist. Acid digestion analysis on the sand found that the concentrations of 20 different metals were detectable, with Fe concentration in the range

of 86.3–184.0 mg/kg. Although the average zeta potential is negative, the sand surface may have positively charged spots due to metal oxides, which leads to favorable retention of CNOs onto this positively charged spots.

4.0 Conclusions

CNOs were cost effectively synthesized by a laser assisted combustion process and characterized by XRD analysis, surface area measurement, and Raman spectroscopic analysis. Sorption experiments revealed that surface oxidized CNOs have higher sorption capacity than C_{60} for metal ion contaminants. CNO aggregates are negatively charged and kept very stable in aqueous suspension under environmentally relevant water chemistry. QCM-D experiments revealed that interactions of CNOs with typical aquifer material surfaces (e.g., iron oxide and silica, under favorable conditions) are electrostatic in origin. Column experiments found that a good control of CNO mobility in porous media is achievable by controlling solution chemistry of injected CNO suspension. The preliminary data suggested that CNOs may serve as a basis to develop innovative in situ remediation technology that is likely more efficient and cost effective. However, additional investigations, such as the sorption kinetics, the stability, and performance of CNOs for repeated removal cycles, and the recovery of CNOs, are necessary for actual remediation design.

References

Burroughs, C., 2000. Sandia scientists study 'natural' alternative to cleaning up uranium contaminated sites: natural attenuation may replace costly traditional remediation techniques. Sandia Lab News, Sandia.

Chen, K., Elimelech, M., 2006. Aggregation and deposition kinetics of fullerene (C_{60}) nanoparticles. Langmuir 22, 10994-11001.

Chen, K., Elimelech, M., 2008. Interaction of fullerene nanoparticles with humic acid and alginate coated silica surfaces: measurements, mechanisms, and environmental implications. Environ Sci Technol 42, 7607-7614.

Chen, X. H., Deng, J. X., Yang, H. S., Wu, G. T., Zhang, X. B., Peng, J. C., Li, W. Z., 2001. New method of carbon onion growth by radio-frequency plasma-enhanced chemical vapor deposition. Chem. Phys. Lett. 336 (3-4), 201-204.

Chen, G. X., Liu, X. Y., Su, C. M., 2011. Transport and retention of TiO(2) rutile nanoparticles in saturated porous media under low-ionic-strength conditions: measurements and mechanisms. Langmuir 27 (9), 5393-5402.

Chen, G. C., Shan, X. Q., Wang, Y. S., Wen, B., Pei, Z. G., Xie, Y. N., Liu, T., Pignatello, J. J., 2009. Adsorption of 2,4,6-trichlorophenol by multi-walled carbon nanotubes as affected by Cu(II). Water Research 43 (9), 2409-2418.

Elimelech, M., 1994. Effect of particle size on the kinetics of particle deposition under attractive double layer interactions. J. Colloid Interface Sci. 164, 190-199.

Elimelech, M., 1991. Kinetics of capture of colloidal particles in packed beds under attractive double layer interactions. J. Colloid Interface Sci. 146 (2), 337-352.

Fortner, J. D., Lyon, D. Y., Sayes, C. M., Boyd, A. M., Falkner, J. C., Hotze, E. M., Alemany, L. B., Tao, Y. J., Guo, W., Ausman, K. D., Colvin, V. L., Hughes, J. B.,

2005. C-60 in water: nanocrystal formation and microbial response. Environ Sci Technol 39 (11), 4307-4316.

Gao, Y., Zhou, Y. S., Park, J. B., Wang, H., He, X. N., Luo, H. F., Jiang, L., Lu, Y. F., 2011. Resonant excitation of precursor molecules in improving the particle crystallinity, growth rate and optical limiting performance of carbon nano-onions. IOP Publishing Nanotechnology 22 165604. http://iopscience.iop.org/0957-4484/22/16/165604.

Katumba, G., Mwakikunga, B. W., Mothibinyane, T. R., 2008. FTIR and Raman spectroscopy of carbon nanoparticles in SiO_2, ZnO and NiO matrices. Nanoscale Research Letters 3, 421-426.

Kaya, A., Yukselen, Y., 2005. Zeta potential of clay minerals and quartz contaminated by heavy metals. Canad. Geotech. J. 42, 1280-1289.

Li, Y. H., Wang, S. G., Luan, Z. K., Ding, J., Xu, C. L., Wu, D. H., 2003. Adsorption of cadmium(II) from aqueous solution by surface oxidized carbon nanotubes. Carbon 41 (5), 1057-1062.

Mauter, M. S., Elimelech, M., 2008. Environmental applications of carbon-based nanomaterials. Environ. Sci. Technol. 42 (16), 5843-5859.

Plonska-Brzezinska, M., et al., 2011. Electrochemical properties of oxidized carbon nano-onions: DRIFTS-FTIR and Raman spectroscopic analyses. ChemPhysChem.

Quevedo, I., Tufenkji, N., 2009. Influence of solution chemistry on the deposition and detachment kinetics of a CdTe quantum dot examined using quartz crystal microbalance. Environ Sci Technol 43, 3176-3182.

Rodriguez-Cabo, B., Rodil, E., Rodriguez, H., Soto, A., Arce, A., 2012. Direct preparation of sulfide semiconductor nanoparticles from the corresponding bulk powders in an ionic liquid. Angew Chem. Int. Ed. 51 (6), 1424-1427.

Roy, D., et al., 2003. Characterization of carbon nano-onions using Raman spectroscopy. Chem. Phys. Lett. 373, 52-56.

Sze, A., Erickson, D., Li, A., 2003. Zeta-potential measurement using the Smoluchowski equation and the slope of the current-time relationship in electroosmotic flow. J. Colloid Interface Sci. 261, 402-410.

Ugarte, D., 1993. Formation mechanism of quasi-spherical carbon particles induced by electron bombardment. Chemical Physical Letters 207 (4-6), 473-479.

U.S. EPA, 2004. Cleaning up the nation's waste sites: markets and technology trends. EPA 542-R-04-015. Environmental Protection Agency, Washington, DC.

Wang, Y. G., Li, Y. S., Fortner, J. D., Hughes, J. B., Abriola, L. M., Pennell, K. D., 2008. Transport and retention of nanoscale C-60 aggregates in water-saturated porous media. Environ. Sci. Technol. 42 (10), 3588-3594.

Wu, C. H., 2007. Studies of the equilibrium and thermodynamics of the adsorption of Cu^{2+} onto as-produced and modified carbon nanotubes. J. Colloid Interface Sci. 311 (2), 338-346.

Yao, K. M., Habibian, M. M., Omelia, C. R., 1971. Water and wastewater filtration – concepts and applications. Environ. Sci. Technol. 5, 1105-1112.

Yang, K., Zhu, L. Z., Xing, B. S., 2006., Adsorption of polycyclic aromatic hydrocarbons by carbon nanomaterials. Environ. Sci. Technol. 40 (6), 1855-1861.

CHAPTER 4

INFLUENCE OF PARTICLE SHAPE ON NANOPARTICLE RETENTION AND RELEASE IN SATURATED POROUS MEDIA

Abstract

Nanoparticle applications have great potentials for environmental remediation; however, there are unknown behaviors of these particles once released into the environment. Engineered and naturally occurring nanoparticles can be found in various shapes including rod-shape carbon nanotubes that have high aspect ratios. The differences in shape could greatly affect the predicted transport and retention in the subsurface. In this work, carboxylate-modified spherical latex particles (average diameter of 210nm) were stretched into rod-shape particles with aspect ratios of 2:1 and 4:1. Scanning electron microscopy (SEM) was used to characterize the size distribution of stretched particles. The measured ζ-potential values of the stretched particles were less negative with increasing aspect ratios. Quartz Crystal Microbalance with Dissipation (QCM-D) experiments were conducted to explore the influence of nanoparticle shape on the interactions of nanoparticles with collector surface under favorable conditions. The retention of nanoparticles in porous media was studied with the use of laser scanning cytometry (LSC) by injecting nanoparticle solution into a microfluidic flow cell packed with glass beads. Analysis of deposition and spatial attachment of spherical and rod-shape particles indicated that particle shape affected transport behavior. Under favorable conditions, spherical particles displayed a higher deposition rate compared to rod-shape particles. Flow cell experiments tested under unfavorable conditions showed the rod-shape particles had a faster attachment rate compared to the spherical particles. It is

likely that a combination of physicochemical and hydrodynamic forces that determine the fate and transport of various shaped particles in porous media. Some additional experiments may be required to ensure the changes in surface charge of the original and stretched particles were not the driving force behind the changes in attachment rates.

1.0 Introduction

Nanotechnology is an emerging science that shows great promise in improving current areas such as medicine, industry, and environmental remediation. A potential use of nanotechnology could be utilized for chemical and physical processes for remediation of toxic chemicals in the subsurface. There is a growing need to improve the efficiency of remediation technologies already present, and the advantages of nano-sized particles could provide these solutions. Studies have been conducted to explore the feasibility of nano zero-valent iron (nZVI) and carbon nanotubes (CNTs) for remediation of contaminated groundwater (Ponder et al., 2000 and Rajan, 2011). Although nanoparticle applications have great potentials, there are unknown behaviors of these particles once released into the environment and this has raised concerns. Knowledge of the fate and transport of nanoparticles in porous media is required to further understand the beneficial uses of nanotechnology and to prevent unintended exposures to the environment.

Many studies have been devoted to exploring the transport and retention of spherical particles in saturated porous media with the use of column studies (Wang et al., 2012; Lecoanet et al., 2004; Ben-Moshe et al., 2010). These studies have helped gain some understanding of various factors influencing transport and attachment including changes in ionic strength, pH value, and particle size. Particle transport in porous media can be more complicated by varying particle and/or collector shape. Classic filtration

theories (Yao et al., 1971) have been based on the behavior of spherical shaped particles; however most nanoparticles and their aggregates are not perfect spheres. Engineered and naturally occurring nanoparticles can be found in various shapes including rod-shape carbon nanotubes that have high aspect ratios (Lecoanet et al., 2004). The differences in shape could greatly affect the predicted transport and retention in the subsurface.

Influence of particle shape on the colloid transport was previously demonstrated (Liu et al., 2010; Xu et al., 2007; Salerno et al., 2006; Toy et al., 2011). Several studies (Salerno et al., 2006; Liu et al., 2010; and Toy et al., 2011) found that particles with higher aspect ratios displayed greater retention compared to spherical particles. Liu et al. found particle transport behavior was affected when comparing spherical particles with diameters of 500 nm to rod-shape particles stretched to aspect ratio of 7.0. However, Xu et al. (2008) concluded the retention was not affected by peanut-shaped colloids when compared to retention measured with spherical particles. Other studies have focused on filterability and transport of bacterial cells with rod-like and spherical shapes (Weiss et al., 1995; Wang et al., 2008; Baltus et al., 2009). Wang et al. (2008) concluded bacterial shape played a role on the filterability of bacterial cells, and Weiss et al.(1995) concluded with column experiments that preferential retention of cells was found with cells with higher aspect ratios. These results conclude transport and retention of particles at the colloid scale are influenced by shape. Previous studies have focused on particles at the colloid scale (micrometer scale), and very little is known about the influence of particle shape at the nanometer scale. Compared to colloids, nanoparticles pose new challenges for scientists. It is already obvious that size plays an important role in the transport and deposition of both colloids and nanoparticles (Auset and Keller, 2004); it is much less

known the role particle shape plays on nanoparticle transport in the environment. Therefore, more research on the effect of shape on transport and retention at the nano-scale is warranted.

Historically, column studies have provided important insights into the retention of nanoparticles in model porous media such as glass beads or Ottawa sands; however, these experiments cannot directly observe the spatial attachment of nanoparticles on collector surfaces. Recently, the technique of LSC has shown to provide the spatial distribution of nanoscale particles in porous media over several pore volumes (May et al., 2012). This technique can prove to be effective in understanding the retention of various shaped nanoparticles in saturated flow conditions.

In this work, the influence of particle shape was explored by evaluating the interactions of nanoparticles with collector surface, using PLL-coated silica sensors under favorable conditions, with QCM-D. The retention of nanoparticles in porous media was studied with the use of LSC by injecting nanoparticle solution into a microfluidic flow cell packed with glass beads. The deposition and spatial distributions of attached nanoparticles were studied under various solution chemistries using spherical particles (average diameter of 210nm) and rod-shape particles, stretched from the spherical particles to aspect ratios of 2:1 and 4:1.

2.0 Materials and Methods

2.1 Model Nanoparticle

Manufactured fluorescent nanospheres (Phosphorex Inc., Fall River, MA) with an excitation maximum at 460 nm and an emission maximum at 500 nm were utilized in this study. These wavelengths were determined to be applicable for use in the Laser Scanning

Cytometer (LSC) and were therefore used throughout all experiments. The stock solution consisted of uniform spheres, with an average diameter of 210 nm, made from polystyrene with a carboxyl surface modification. The density of the particles was reported by the manufacturer as 1.06 g/cm^3. The purchased particles were used as spheres as obtained from the company or physically stretched into desired rod-like shapes with aspect ratios of 2:1 and 4:1.

2.2 Stretching of Nanoparticles

The method of stretching the spherical nanoparticles into rod-shape particles was conducted according to the method published by Champion et al. (2007), based on a previously developed technique by Ho et al. (1993). Briefly, 1 to 2 mL of nanoparticles, comprised of 2.5 % solids, was introduced into a solution of 10 % (wt/vol) polyvinyl alcohol (PVA)/water. Glycerol was added to aid in the stretching process and the solution was poured onto a drying plate. After allowing time to dry completely (approximately 24-48 hours depending on humidity and room conditions), a film was created which was then placed into a stretching apparatus (Appendix D, Figure D.5) and submerged into a mineral oil bath at a temperature of 125 ˚C. This temperature is approximately the "glass transition temperature" (or softening point) of the polystyrene particles, which allowed the particles to form into the desired shape created during the stretching process. After the stretching process, the film was dissolved and the particles were cleaned and extracted with centrifugation (Eppendorf Centrifuge 5804R). A more detailed procedure is presented in Appendix A, Section A.1. The concentrations of the stretched nanoparticles were determined using UV-Vis spectrophotometry (UV-3101PC, Shimadzu Corporation, Columbia, MD), by creating a calibration curve with known concentrations

of spherical particles provided by the manufacturer. A lyophilizer (Lyph-Lock 12 Freeze Dryer, Labconco, Kansas City, MO) was also used to verify concentration method of UV-Vis spectrophotometry. A known volume of nanoparticle stock solution was measured and placed into the lypholizer. After allowing the solution to freeze dry overnight, the dry mass of the nanoparticles were weighed and a concentration was determined. This method resulted in similar concentrations measured with the UV-Vis spectrophotometer.

2.3 Model Porous Media

Spherical glass beads (Potters Industries, Inc., Valley Forge, PA) were chosen as model porous media for the flow cell experiments. The glass beads have a density of 2.5 g/cm^3 and were sieved with a 25 U.S. sieve, resulting in a maximum diameter of 710 μm and a minimum diameter of 600 μm. Prior to use, the glass beads were washed to remove any impurities by following a procedure reported in Wang et al (2008). The electrophoretic mobility of the glass beads were measured using a ZetaPALS analyzer (Brookhaven Instruments Corporation, Holtsville, NY) according to the procedure reported by Kuznar and Elimelch (2007). A detailed procedure for washing and analyzing the electrophoretic mobility and subsequent ζ-potential of the glass beads are presented in Appendix A, Section A.2 and A.3.

2.4 Characterization of Nanoparticles

Scanning electron microscopy (SEM; FEI model Quanta 200 FEG) was used to produce images of the rod-like and spherical particles. Samples were first sputter-coated (Cressington 108 Auto Sputter Coater) with a Platinum/Palladium mixture. The images were analyzed with digital imaging software (Museum of Science, Boston MA) to

determine the major and secondary axes of both the 2:1 and 4:1 rod-shaped particles. The average hydrodynamic radius of the spherical particles, under varying solution chemistry, was obtained by dynamic light scattering (DLS) with the use of the Zetasizer Nano ZS (Malvern Instruments, Southborough, MA). The electrophoretic mobility (EPM) and the ζ-potential of the spherical and rod-shaped particles with varied ionic strength were also obtained using the Zetasizer.

The surface area was calculated to compare the stretched particles to the spherical particles. The surface area (S) of the stretched rod-like particles was approximated using Equation 1 (Liu et al. 2010).

$$S = 2\pi c^2 + \left(\frac{2\pi ca}{e}\right) sin^{-1}e \quad (1)$$

Where *c* is the secondary axis radius, *a* is the major axis radius, and *e* is the ellipticity of a rod-like particle, calculated by using Equation 2 (Liu et al. 2010). The effective radius (a_{eff}) of the rod-like particles was also found by calculating the radius of a sphere that would have the same surface area as the rod-shape particles, shown in Equation 3.

$$e = \sqrt{1 - \frac{c^2}{a^2}} \quad (2)$$

$$a_{eff} = \sqrt{\frac{S}{4\pi}} \quad (3)$$

2.5 Interaction Energy Profile

The interaction energy between the nanoparticles and planar surfaces (glass beads) were calculated using the classical Derjaguin-Landau-Verway-Overbeek (DLVO) theory. The theory describes the interaction as a sum of the van der Waals (generally

attractive) and electric double-layer (generally repulsive) interactions. For the evaluation of interaction energy in this study, expressions developed by Guzman et al., (2006) were utilized. Equations used for calculations are presented in Appendix B. The measured radius for the spherical particles was utilized in the equations, and the calculated effective radius was used for the rod-shape particles.

2.6 QCM-D Experiment

Deposition experiments, with varied solution chemistry, were conducted with the use of a quartz crystal microbalance with dissipation (QCM-D) E-1 unit (Q-Sense, Sweden) with a silica coated sensor surface (QSX 303). Favorable conditions were created on the originally negatively charged sensor by modifying the sensor surface with positively charged poly-L-lysine (PLL) poly-electrolyte (Sigma Aldrich, St. Louis, MO) solution, a similar method was used in previous studies (Chen and Elimelch, 2006, 2008). The sensor surface was cleaned according to the recommended protocol by the manufacturer prior to each experiment, and duplicate tests were conducted. For all experiments, the flow rate was 0.100 (± 0.001 mL/min) and a temperature of 22 ˚C was set. The sensor surface was first equilibrated with DI water until the shift in the third overtone frequency (Δf_3) was less than 0.5 Hz for 10 min. Next, the sensor surface was prepared with a "PLL-free" buffer solution consisting of 10 mM HEPES (Sigma-Aldrich, St. Louis, MO) and 100 mM NaCl. A 0.1 g/L PLL solution was then flowed through the chamber until stabilized, followed by a rinse with background solution consisting of the electrolyte of interest (3 to 100 mM NaCl and 0.1 to 10 mM $CaCl_2$). Finally, a solution of nanoparticles in electrolyte of interest was flowed across the modified sensor surface. When the particles deposited onto the sensor, a shift in the overtone frequency (Δf_n)

resulted due to a change in mass. The change in frequency of the third overtone (Δf_3) was analyzed to determine the initial deposition rate (r_d) over the time period tested (dt), as shown in Equation 4. A detailed procedure and QCM-D schematic is provided in Appendix C.

$$r_d = \frac{d\Delta f_3}{dt} \quad (4)$$

2.7 Flow Cell Experiment

To quantify the spatial distribution of spherical and rod-shaped particles in porous media, microfluidic flow cell experiments were conducted by using Laser Scanning Cytometry (LSC, CompuCyte Corporation, Westwood, MA) as previously used to analyze nanoparticle attachment (May et al., 2012). The LSC incorporates fluorescent microscopy and flow cytometry technologies to analyze the distribution of nanoparticle transport and attachment at a centrimetre scale. A 50 mm long, 5 mm wide, and 0.8mm deep flow cell (ibidi μ-Slide $I^{0.8}$ Luer, Ibidi LLC, Verona, WI) designed for high resolution microscope analysis was packed with a single layer of spherical glass beads (porosity near 0.45). The inlet and outlet of the flow channel was connected with TYGON 3350 sanitary silicone tubing with a 1/16 inch inner diameter (Saint-Gobain Performance Plastics Corporation, Beaverton, MI) to a syringe pump (KD Scientific, Inc., Holliston, MA). A schematic of the flow cell design and LSC equipment is presented in Appendix C, Figure C.2. Prior to each experiment, the flow cell was saturated with a background solution consisting of the electrolyte of interest. Next, the desired pore volume (PV) of nanoparticle solution was injected under various conditions, followed by 10 PV of background solution. Finally, a domain of 12 mm long and 5 mm wide in the middle section of flow cell was scanned using LSC.

To first observe any changes due to particle shape, a series of pore volumes (10, 20, 40, & 80 PV) were injected with spherical and rod-shape (2:1) nanoparticle solution at a concentration of 0.00025% solids in 3 mM NaCl and pH 7.0. Next, a direct injection of 80 pore volumes of spherical and rod-shape (2:1) & (4:1) nanoparticle solution at a concentration of 0.00025% solids in 3 mM NaCl and pH 7.0 & 11.0 to observe the influence of collector heterogeneity. Finally, a long injection time of 350 pore volumes of spherical and rod-shape (2:1) & (4:1) nanoparticle solution at a concentration of 0.0025% solids in 3 mM NaCl and pH 7.0 was tested to explore the attachment of each particle shape over time. All experiments were tested with a Darcy velocity of 0.04 cm/s.

3.0 Results and Discussion

3.1 Characterization of Nanoparticles

During the stretching process, the surface area of the nanoparticles increased while the volume was held constant. SEM images confirmed the aspect ratios for the stretched particles and are presented in Figure 1.

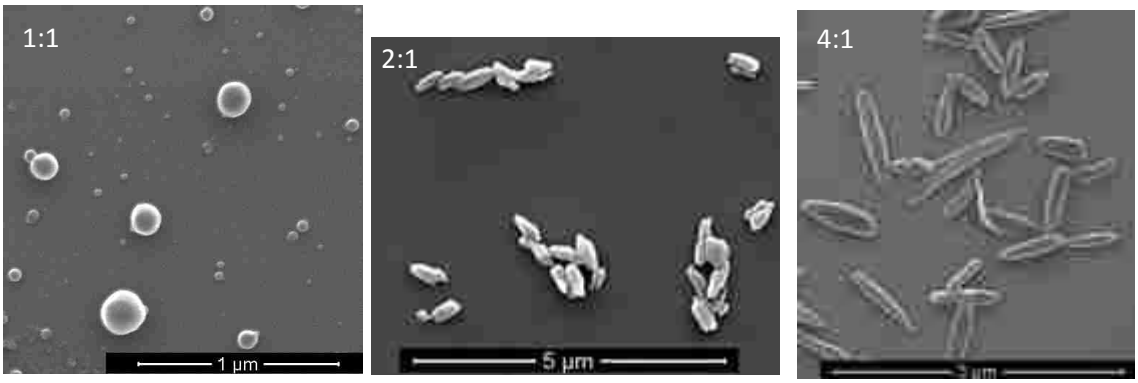

Figure 1. Scanning electron microscopy images of spherical (1:1), stretched rod-shape (2:1), and stretched rod-shape (4:1) particles.

Digital analyzing software (Digital Earth Watch, Pickle & Kirtley, Museum of Science, Boston, MA) was used to measure the dimensions of one hundred stretched nanoparticles collected in SEM images. The longest distance for the length (major axis) and width (secondary axis) of the particles were measured from edge to edge using the software and the scale given in the SEM image. Particles stretched to aspect ratio of 2:1 were measured to have a ratio of 2.3:1, and particle stretched to 4:1 were measured with a ratio of 3.6:1.The major and secondary axis radii for the rod-shape particles were determined as the average diameters obtained from the one hundred particles measured with the digital imaging software. The particle diameter distribution for the major and secondary axis for the 2:1 and 4:1 rod-shape particles are presented in Figure 2. The particle distribution for the stretched 2:1 rod-shape particles ranged from 250 to 750 nm for the major axis with the average at 400 to 450 nm, shown in Figure 2A. The secondary axis ranged from 120 to 320 nm with an average diameter at 200 to 220 nm, shown in Figure 2B. The stretched 4:1 rod-shape particles displayed an average particle dimension of 800-850 nm for the major axis diameter and 240-260 nm for the secondary axis diameter, shown in Figure 2C and 2D, respectively. The distribution of the major and secondary axis diameter for the 4:1 rod-shape particles had a greater range with particles from 450 to 1200 nm and 100 to 400 nm, respectively.

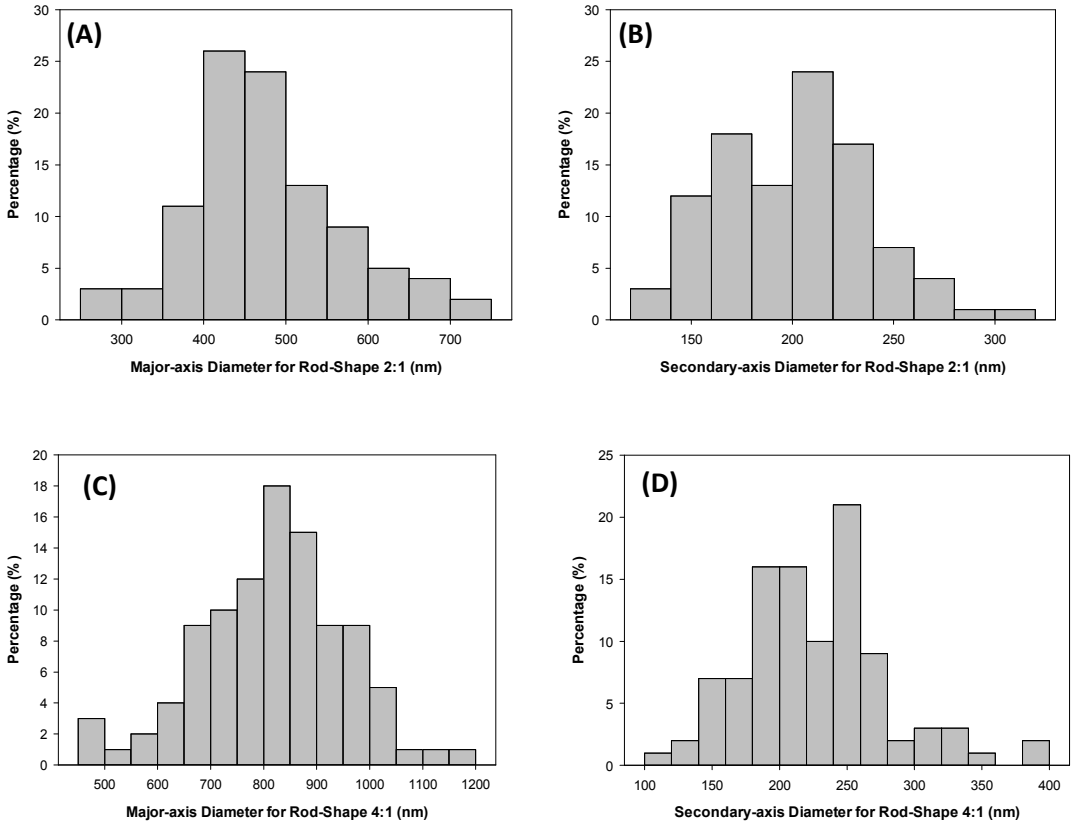

Figure 2. Particle diameter distributions for stretched rod-shape (A) 2:1-major axis, (B) 2:1-secondary axis, (C) 4:1-major axis, and (D) 4:1-secondary axis particles.

Table 1 displays measured and calculated particle characteristics for all three of the tested particles. The calculated particle surface area increased from 0.14 to 0.25 and 0.40 μm^2 for spherical, rod-shape (2:1 aspect ratio), and rod-shape (4:1 aspect ratio), respectively. After the stretching process, the calculated effective radius increased from 0.105 to 0.14 and 0.18 μm for spherical, 2:1 aspect ratio, and 4:1 aspect ratio, respectively. The effective radius was used in DLVO calculations for non-spherical particles.

Table 1. Particle characteristics for spherical and stretched particle with aspect ratios of 2:1 and 4:1.

Particle Characteristic	Spherical	Rod-shape (1)	Rod-shape (2)
Aspect Ratio	1:1	2:1	4:1
Surface area, μm^2	0.14	0.25	0.40
Major-axis radius, μm	0.105	0.2385	0.4
Secondary-axis radius, μm	0.105	0.1	0.1
Ellipticity	0	0.91	0.97
Effective radius, μm	0.105	0.14	0.18

Figure 3 and Figure 4 shows the ζ-potential measurements for the spherical and stretched particles over varying ionic strengths of NaCl and $CaCl_2$, respectively. The measured ζ-potentials for the spherical and stretched particles were found to have slight differences with the stretched particles being less negative. The spherical particles have a range of ζ-potentials from -50 to -33 mV from 3 to 200 mM NaCl, respectively. The ζ-potential measurements for the rod-shape (2:1) particles range from -40 to -16 mV for 3 to 200 mM NaCl, respectively and particles with aspect ratio 4:1 displayed less negative values with ζ-potentials ranging from -24 to -14 mV for 3 to 50 mM NaCl, respectively. The same trend of decreasing ζ-potential was observed with spherical and 2:1 stretched particles under varying ionic strengths of $CaCl_2$. A sharp decrease in ζ-potential was observed between 0.1 to 2 mM $CaCl_2$ and became more stable at higher ionic strengths. Previous studies using similar processes to stretch spherical particles have reported no significant changes in ζ-potential measurements (Salerno et al., 2006) while other studies have reported slight changes (Liu et al., 2010; Ho et. al., 1997 & 1998). Changes in ζ-potentials in this study are slightly greater for spherical to rod-shape particles (4:1) compared to those reported by Liu et al. (2010) for spherical particles stretched to aspect ratio 7:1. The particles used in this study were smaller with spherical particles starting

with a diameter of 210 nm compared to Liu et al. (2010) studies where spherical particles where 500 nm and stretched to a higher aspect ratio. The greater changes in ζ-potential for this study could be attributed to the smaller size of particles tested. Another reason for the change in ζ- potentials of the stretched nanoparticles could be a result from residual amounts of poly(vinyl-alcohol) (PVA) adsorbed to the colloid surface during the stretching procedure. Control spherical particles were tested by first incorporating the spherical particles into a PVA film then extracting the particles without stretching. The ζ-potential of these particles in DI water at pH 7.0 was found to be -53 mV and -46 mV for control particles in 3 mM NaCl at pH 7.0. As shown in Figure 3, spherical particles that were not introduced into a PVA film had a ζ-potential near -52 mV for DI water and -50 mV for 3 mM NaCl. The change in ζ-potential was not very significant in DI water but changed slightly as the ionic strength increased. Electrophoresis performed by Ho et. al. (1997) found that the ζ-potential changed with aspect ratio for the smallest particles (spherical particles with diameter of 208 nm stretched to reported axial ratio of 1.93) and when comparing stretched to un-stretched particles that were not exposed to the PVA film. They hypothesized the charge could be larger on the ends of the stretched particles, but analyzed the charge distribution and concluded that the stretching procedure did not create any surface charge non-uniformity (Ho et. al., 1997).

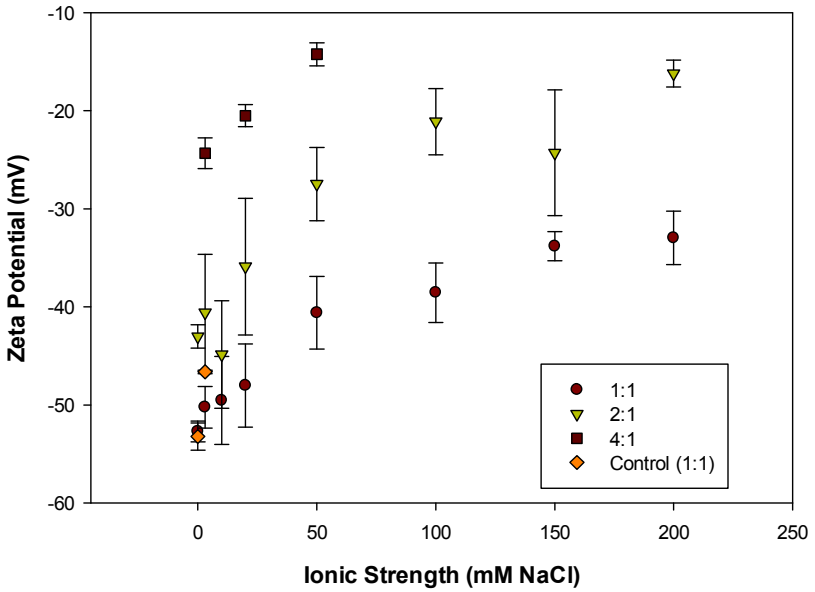

Figure 3. Effects of Ionic Strength of NaCl on Zeta Potential measurements for spherical and rod-shape particles.

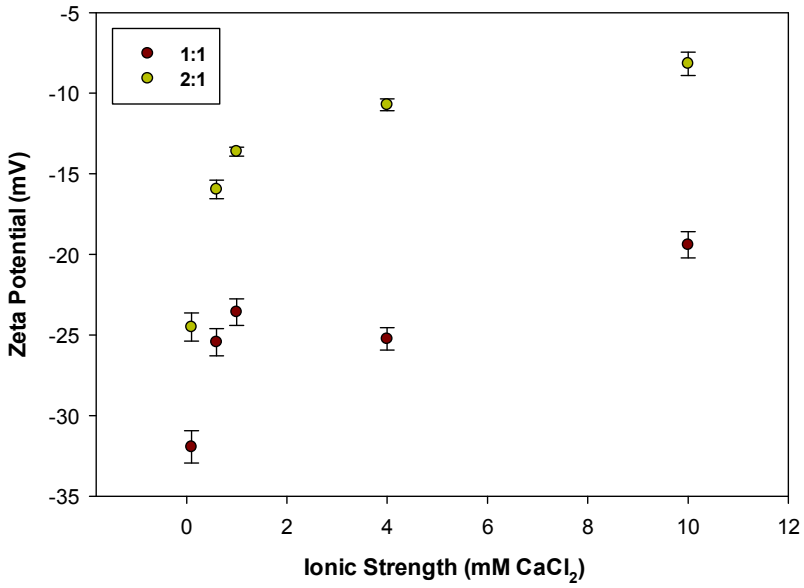

Figure 4. Effects of Ionic Strength of $CaCl_2$ on Zeta Potential measurements for spherical and rod-shape particles.

3.2 Interaction Energies

The ζ-potentials of the glass beads and particles were used to determine the interaction energy profile as a function of ionic strength of NaCl at pH 7.0. The glass beads and nanoparticles were both negatively charged. The glass beads' ζ-potential increased from -46.81 mV to -19.39 mV, when the ionic strength increased from 3 to 100 mM NaCl. The increase of ionic strength seemed to have more of an effect on the increase of measured ζ-potentials for the glass beads compared to spherical nanoparticles where the ζ-potentials increased from -50.23 mV to -38.56 mV for ionic strengths from 3 to 100 mM NaCl.

All interaction energy profiles examined for the particle-glass bead system displayed a large energy barrier under low ionic strength conditions (3 mM NaCl) and decreased with increasing ionic strength (50 to 100 mM NaCl). As the aspect ratio of the stretched particles increased, the energy barrier became more sensitive (decreases more quickly) with increasing ionic strength. Table 2 displays the heights of energy barriers and the depths of secondary minima for all tested particle-glass bead systems. The interaction energy profile for the spherical nanoparticle-glass bead system, shown in Figure 5 indicates a repulsive energy barrier and a small secondary energy minimum well for all ionic strengths tested. The energy barrier is reduced from 285 kT to 3.9 kT and the secondary energy well become more evident with increasing ionic strength from 3 to 100 mM NaCl. Therefore increasing ionic strength should favor more attachment for the spherical particles onto the glass beads. Figure 6 shows a similar trend of interaction energies for the stretched (2:1) particle-glass bead system, where a repulsive energy barrier from 290 kT to 30 kT is present for ionic strengths of 3 to 50 mM NaCl; however

unlike the energy barrier for the spherical particles, the energy barrier disappeared at ionic strength of 100 mM NaCl for the stretched (2:1) and the secondary minimum is no longer evident, therefore at an ionic strength of 100 mM NaCl stretched (2:1) particles could easily attach to the glass bead surface. Interaction energies analyzed for the stretched (4:1) particles-glass bead system, Figure 7, display an energy barrier from 158 kT to 51 kT for 3 and 20 mM NaCl, respectively and disappear with 50 mM NaCl, indicating favorable attachment at 50 mM NaCl.

Table 2. Calculated interaction energy barriers heights and depths of secondary minima for spherical and rod-shape particles.

	Spherical	Rod-shape (2:1)	Rod-shape (4:1)
Energy barrier in 3 mM NaCl (kT)	285	290	158
Energy barrier in 20 mM NaCl (kT)	124	113	51
Energy barrier in 50 mM NaCl (kT)	51	30	-1.58
Energy barrier in 100 mM Nacl (kT)	3.89	-1.13	--
Secondary minimum in 3mM NaCl (kT)	-0.29	-0.49	-0.80
Secondary minimum in 20 mM NaCl (kT)	-1.66	-2.58	-4.04
Secondary minimum in 50 mM NaCl (kT)	-3.65	-5.74	-1.58
Secondary minimum in 100 mM NaCl (kT)	-6.70	-1.13	--

Figure 8 compares the interaction energies for all three tested particles at 3 mM NaCl and pH 7.0. Energy profiles for spherical and stretched (2:1) particles are similar with peaks near 280 kT, however the stretched (4:1) particles display a much lower energy barrier near 160 kT. This indicates more attachment is likely with the stretched (4:1) particles in comparison to the spherical and stretched (2:1) particles. Since the rod-shape interaction energies profiles were created by using the effective radius (a_{eff}), there may be differences on the actual interaction of the particles and glass beads based on the orientation of the rod-shape particles (major or secondary axis) relative to the glass bead.

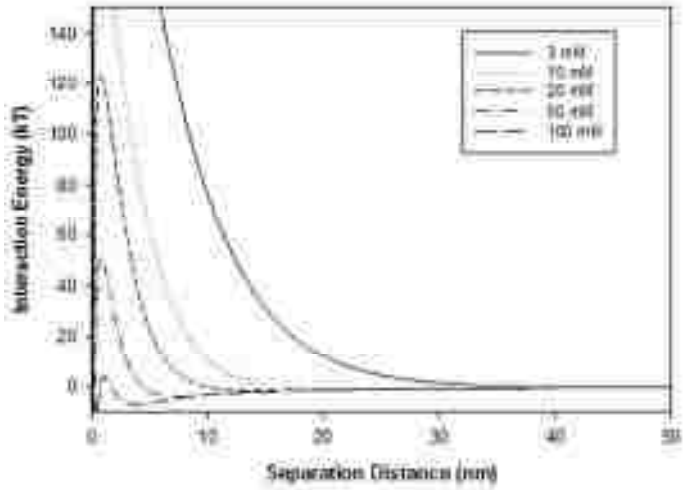

Figure 5. Interaction energy profile for spherical (1:1) nanoparticle-glass bead system.

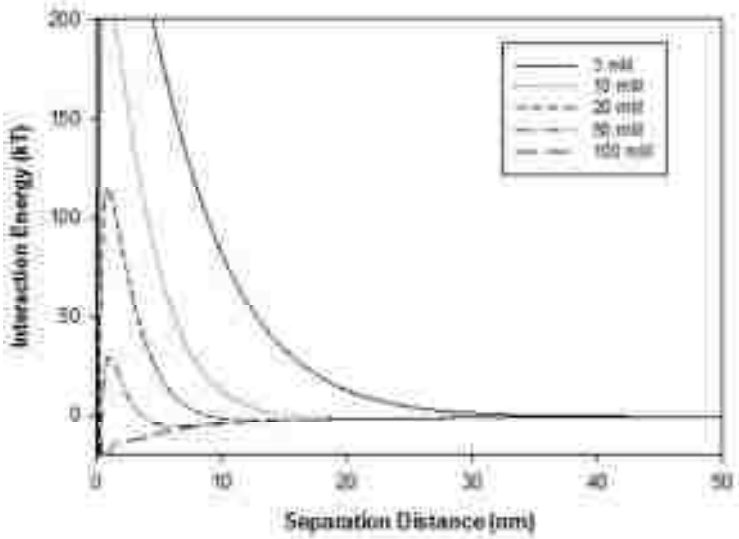

Figure 6. Interaction energy profile for rod-shape (2:1) nanoparticle-glass bead system.

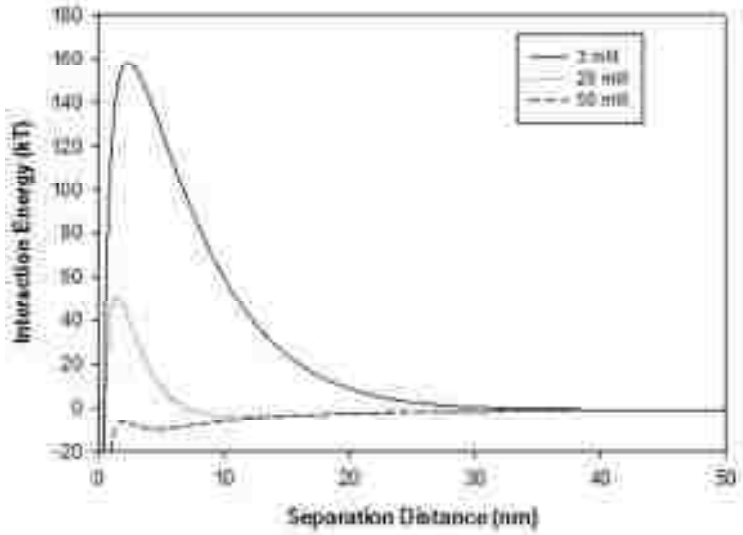

Figure 7. Interaction energy profile for rod-shape (4:1) nanoparticle-glass bead system.

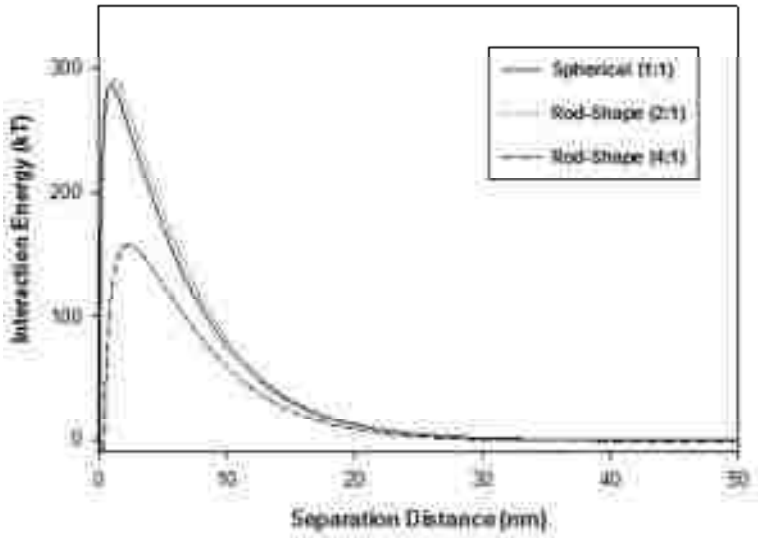

Figure 8. Interaction energy profile for spherical and rod-shape nanoparticle-glass bead system under 3 mM NaCl.

3.3 Deposition under favorable conditions

QCM-D studies were first conducted using bare silica sensor surface (negatively charged) and iron-oxide sensor surface (slightly positively charged under conditions tested) at a pH of 7.0 which led to no observed deposition. It is expected that no

deposition should occur when both nanoparticles and surfaces are negatively charged. No deposition onto silica surface indicates minimal charge heterogeneity on the surfaces of nanoparticles and silica surface. The isoelectric point for iron oxide is near a neutral pH value, so the positive charge of the iron-oxide sensor under the tested conditions (pH 7.0) may be very weak. Further QCM-D studies focused on favorable conditions (negative particle surface charge and positively charged sensor surface), which were created by coating bare silica sensor surfaces with a positively charge polymer PLL, following procedure by Chen and Elimelech, 2006. QCM-D experiments, with spherical and rod-shape (2:1 & 4:1) nanoparticles, were conducted under varying ionic strengths (3 to 100 mMNaCl and 0.1 to 10 mM $CaCl_2$) where nanoparticles are relatively stable.

Figure 9 shows the deposition rate (Hz/min) of the spherical and rod-shape nanoparticles onto PLL-coated silica sensors under varying ionic strengths of NaCl. The spherical particle's deposition rate decreased from approximately 14 to 8 Hz/min for ionic strengths of 3 to 100 mM NaCl. The rod-shape particles (2:1 & 4:1) showed a much lower deposition rate that remained relatively constant at approximately 2.0 and 1.0 Hz/min, respectively, across the same ionic strengths. This decrease in deposition rate with increasing ionic strength for the spherical particles is consistent with the DLVO theory of colloidal stability. As the negatively charged nanoparticles approach the positively charged sensor surface (under favorable conditions) at short distances, the electric double layer and van der Waals forces are both attractive (Elimelech 1991 and 1994). As the ionic strength increases, the double layer will decrease which leads to a reduced deposition rate. The rod-shape particle's deposition rate was not sensitive to increasing ionic strength and does not follow the previously discussed theory. Previous

work by Adamczyk and Weronski (1998) with non-spherical particles found with increasing particle aspect ratio, there was a decrease in the effective interaction range in relation to the particle double layer thickness. This may cause an observed lower deposition rate for rod-shape particles at lower ionic strengths compared to spheres and the insensitivity to ionic strength. Deposition results with varying $CaCl_2$ also showed greater deposition rate with spherical particles compared to rod-shape (2:1) and decreased with increasing ionic strength for spherical particles only, shown in Figure 10.

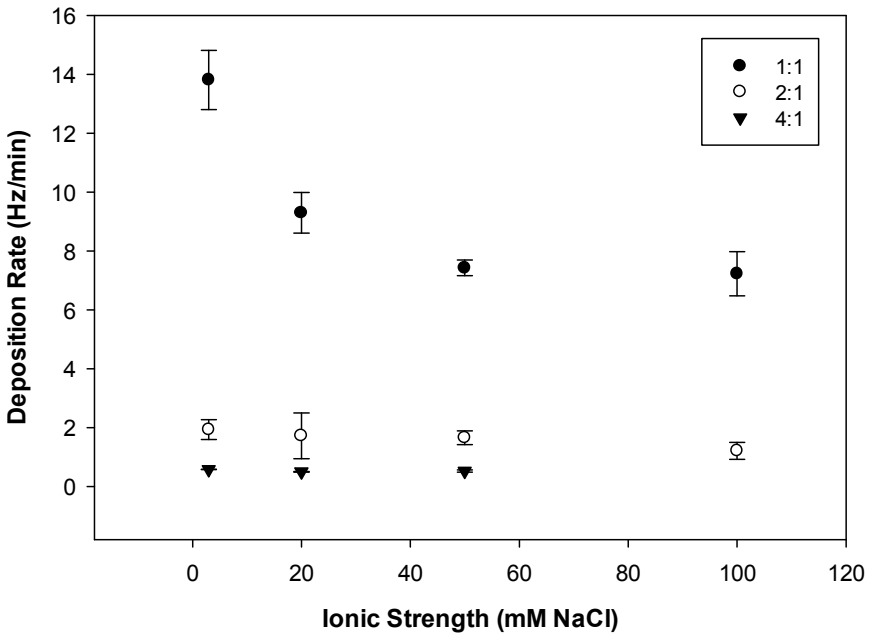

Figure 9. Influence of ionic strength of NaCl on spherical and rod-shape particle deposition on PLL-coated silica sensor.

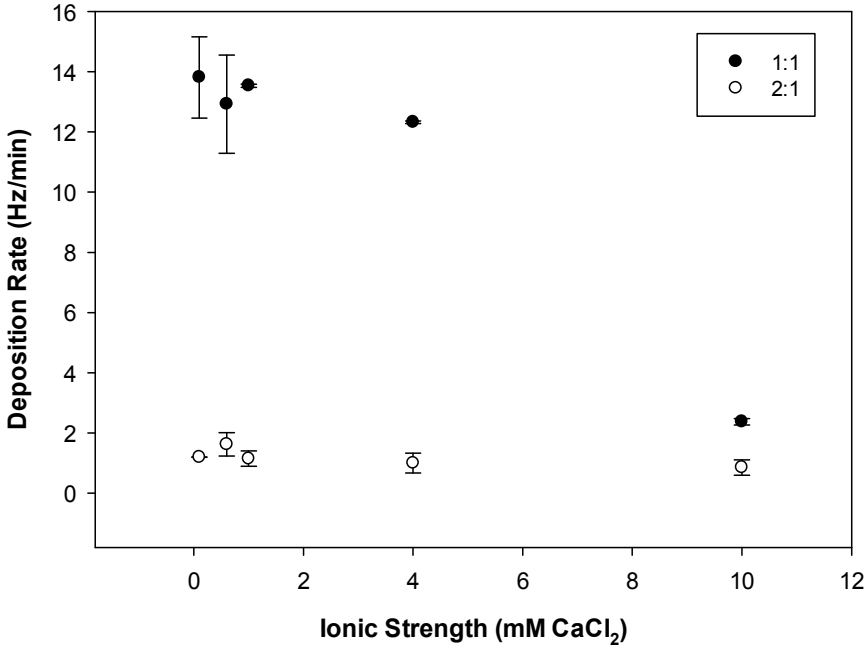

Figure 10. Influence of ionic strength of $CaCl_2$ on spherical and rod-shape particle deposition on PLL-coated silica sensor.

3.4 Distribution of Spherical and Rod-Shape Nanoparticles

Flow cell experiments explored the transport and attachment of the spherical and rod-shape nanoparticle in the model porous media. The distribution of attached particles obtained from LSC was analyzed using MATLAB by generating scan areas in the middle of the flow cell (from 19 to 31 mm away from the inlet). Due to vertical clearance on the LSC microscope and the inlet and outlet on the flow cell, only the middle section of the flow cell was able to be scanned. The first flow cell test was conducted over a series of pore volume injections (10, 20, 40, & 80 PV) in order to observe the changes of nanoparticle distribution over time. This was done with 0.00025 % solids nanoparticle solution with spherical and stretched (2:1) particles with pH 7.0 and varying solution chemistry of 0, 3, and 50 mM NaCl. Using various conditions of ionic strength and pore volume injections was conducted initially in order to observe any possible changes in

attachment between spherical and rod-shape particles and also to determine if attachment was sensitive to changes in ionic strength. The results for all tested pore volume injections (presented in Appendix E) displayed a greater increase in particle attachment with increasing pore volumes for the stretched (2:1) particles compared to spherical. It was also found that very little attachment was observed with 0 mM NaCl (only DI water) for both spherical and stretched (2:1). Under conditions of 50 mM NaCl, the attachment was relatively close to the attachment observed with 3 mM NaCl; therefore the remaining experiments were conducted with only 3 mM NaCl to simulate conditions relevant with the environment. It was concluded that 80 PV injections showed significant attachment from the previous results and was used to explore the influence of shape for all three particles tested.

Figure 11 shows an LSC scan after 80 PV injection of 0.00025 % solids nanoparticle solution in 3mM NaCl (pH 7.0) for spherical, rod-shape (2:1), and rod-shape (4:1) followed by 10 PV of background solution (3mM NaCl, pH 7.0). The color bar on each figure represents the amount of fluorescence detected during the scan. The higher the amount of fluorescence correlates to more attachment of nanoparticles. As displayed in the figure, as the aspect ratio of the nanoparticle increases, the attachment of the particles to the glass beads increase. There are more red dots, correlating to more fluorescence and therefore more particles, found in Figure 11c for the rod-shape (4:1) particles. This finding is consistent with column experiments by Salerno et al. (2006) where measured retention increased with aspect ratio for slightly larger spherical particles with average diameter 500 nm and stretched particles with primary axis measurements of

850 nm and 1.06 μm. Another study by Weiss et al. (1995) found bacterial cells with higher aspect ratios had increased retention in columns packed with quartz sand.

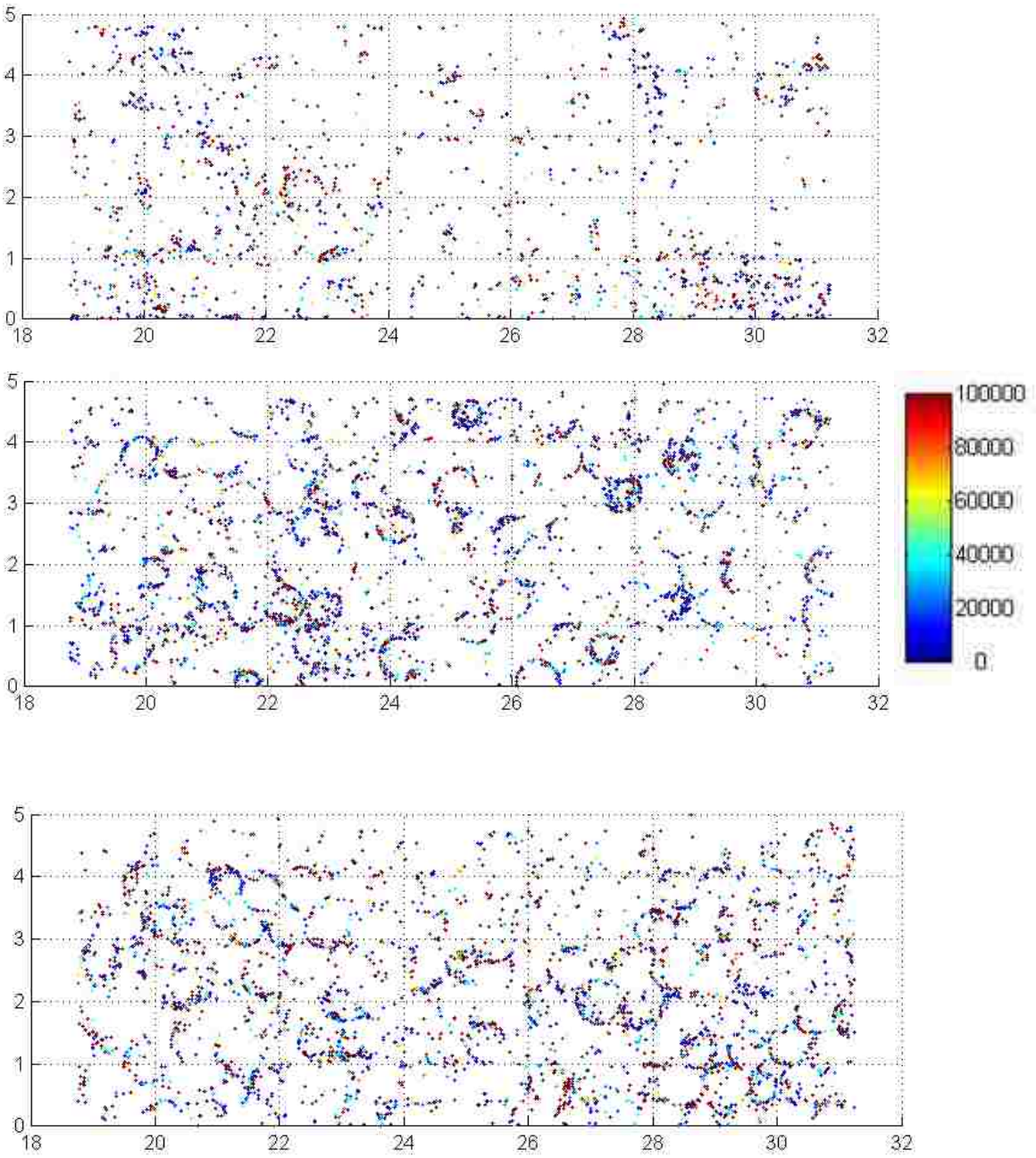

Figure 11. Distribution of detected fluorescence from attached nanoparticles at 3mM NaCl, pH 7.0, 80 PV of 0.00025 %solids nanoparticle suspension of (A) spherical particles, 1:1 (B) Rod-shape, 2:1 and (C) Rod-shape, 4:1, followed by 10 PV of background solution.

Here, the particles and glass beads are both negatively charged. According to the DLVO energy analysis (Figure 8), a sizable energy barrier of 280 kT for spherical and rod-shape (2:1) and 160 kT for rod-shape (4:1) exists between particle and glass bead surfaces, which should theoretically prevent any attachment from occurring. Particle attachment, however, was clearly shown for all particle shapes.

The stability of attachment was examined by injecting 10 PV of DI water after the initial scan of attached nanoparticles. Theoretically, if nanoparticles were attached in the secondary minimum well, they are only loosely associated with the glass bead surfaces; therefore flushing of DI water would significantly mobilize the attached nanoparticles. Figure 12 shows a comparison of LSC scan of 80 PV of rod-shape (2:1) nanoparticles before and after the additional 10 PV of DI water. Clearly, very similar amount of fluorescence were detected before and after DI water, indicating that the attachment was very stable and that secondary minimum played a minor role on the nanoparticle attachment.

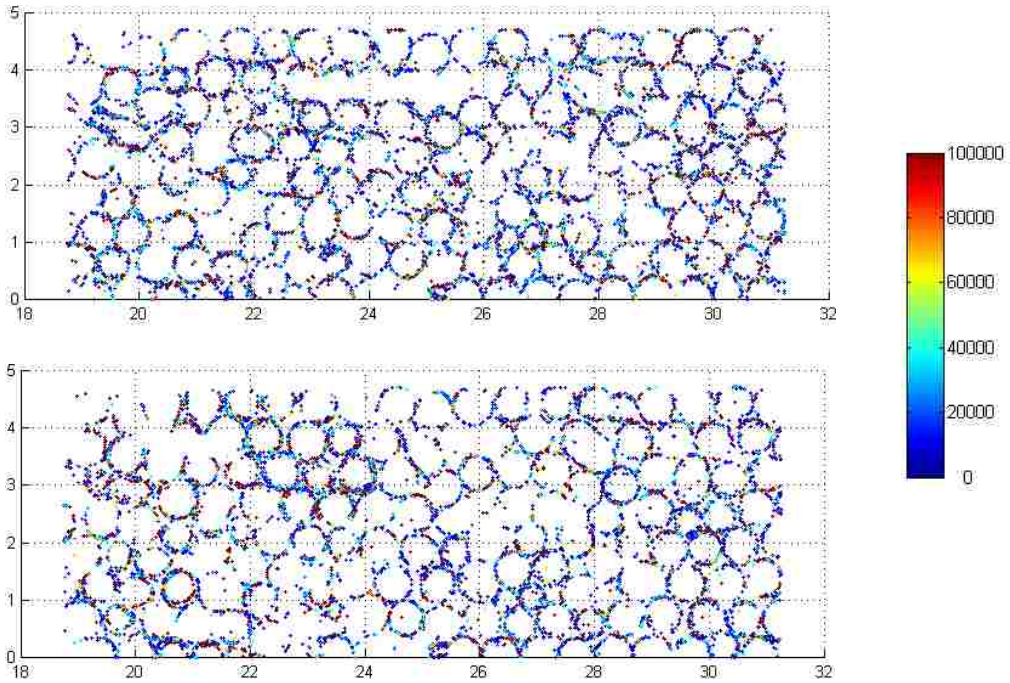

Figure 12. Distribution of detected fluorescence at 3mM NaCl, pH 7.0, 80 PV of 0.00025 % solids (2:1) nanoparticle suspension (A) before DI and (B) after DI flush.

The observed stable attachment is contrary to observations with unfavorable conditions tests with QCM-D studies, where deposition did not occur with negatively charged particles and negatively charged bare silica sensors. We hypothesize that attachment shown in LSC studies was due to the surface heterogeneities of the glass beads. The glass beads were purchased from the manufacturer and washed to remove impurities; however some metal oxides may still be present. Figure 13 displays an SEM image collected of the beads showing they are not homogeneous and the surfaces of the beads have rough areas where deposition may be more favorable.

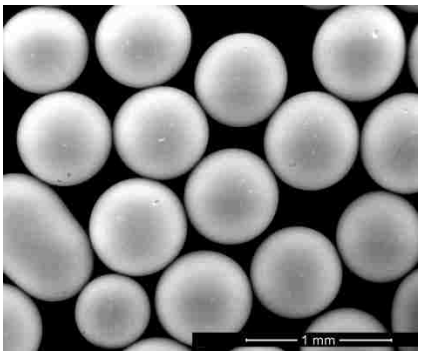

Figure 13. Scanning electron microscopy image of glass beads.

Various metal oxide impurities (Al_2O_3, MgO, Na_2O, CaO, and Fe_2O_3) have been reported on the surface of glass bead collectors (Litton and Olsen, 1993). At pH 7.0 (used in all previous experiments), the metal oxides present on the surface of the beads would have a neutral or slightly positive charge compared to the negative charge of the particles; therefore providing favorable or fast attachment rates. To eliminate the influence of these metal oxides on the attachment of particles onto the glass beads, tests were conducted for spherical and stretched (2:1) particles under conditions of pH 11.0 and 3 mM NaCl. At this higher pH, the surface impurities will carry a negative charge since it is near their isoelectric point. An obvious decreasing trend in total measured fluorescence was observed for both the spherical and stretched (2:1) particles as shown in Figure 14. The total fluorescence measured for spherical particles decreased from 6.82×10^8 to 2.61×10^8 and total fluorescence for rod-shape (2:1) decreased from 7.42×10^8 to 6.17×10^8. This shows that chemical heterogeneity may be playing a significant role in the attachment of negatively charged particles onto the glass beads. It is also shown that the decrease in measured fluorescence with an increase in pH is more apparent with the spherical particles decreasing approximately 3.5 times more than the rod-shape particles.

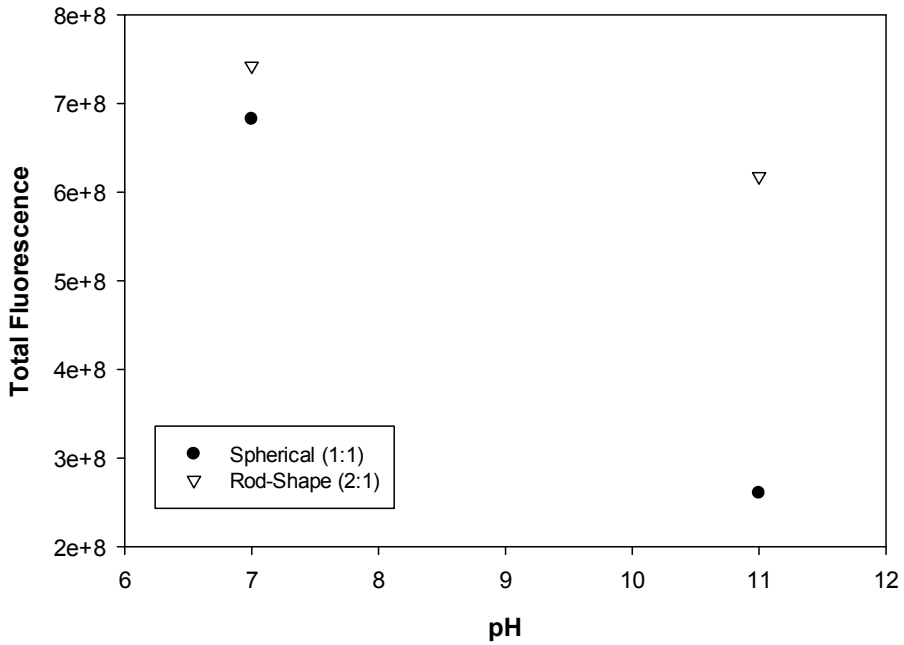

Figure 14. Influence of pH on the measured total fluorescence of attachment spherical and rod-shape (2:1) particles on glass beads.

To further explore the increased amount of attachment of rod-shape particles in comparison with spherical particles, a long injection time of 350 PV for all three tested particles was conducted under 3 mM NaCl and pH 7.0 conditions. Figure 15, shows images produced for the LSC for 350 PV injections for spherical, rod-shape (2:1), and rod-shape (4:1), respectively. Although clearly less attachment was observed for spherical particles than rod-shape shapers after 80 PV of injection (Figure 11), the difference in the total amount of attachment was less evident after 350 PV. This suggests that it is not that the glass beads possess higher retention capacity for the rod-shape particles, so that they showed more attachment after 80 PV. It is possible that the rod-shape particles initially have higher attachment rate, so that more attachment was observed after 80 PV of injection. As more particles took the available spots on the glass surface, the attachment rate will be reduced. After longer injection period (e.g. 350 PV),

the amount of the particles attached on the surface is closer to the maximum retention capacity, so that the difference is reduced. Higher initial attachment rate of rod-shape particles may be attributed to the fundamental different motions of these particles. For example, attachment of spherical particles is not influenced by the orientation of each particle. However, orientation of each rod-shape particle will greatly influence the interaction with glass bead surfaces. Particles might be more favorable to be attached under either end-on or side on orientation. In this study, all the particles have same volume, but rod-shape particles should have higher surface area, which might also increase the possibility of attachment during the transport process.

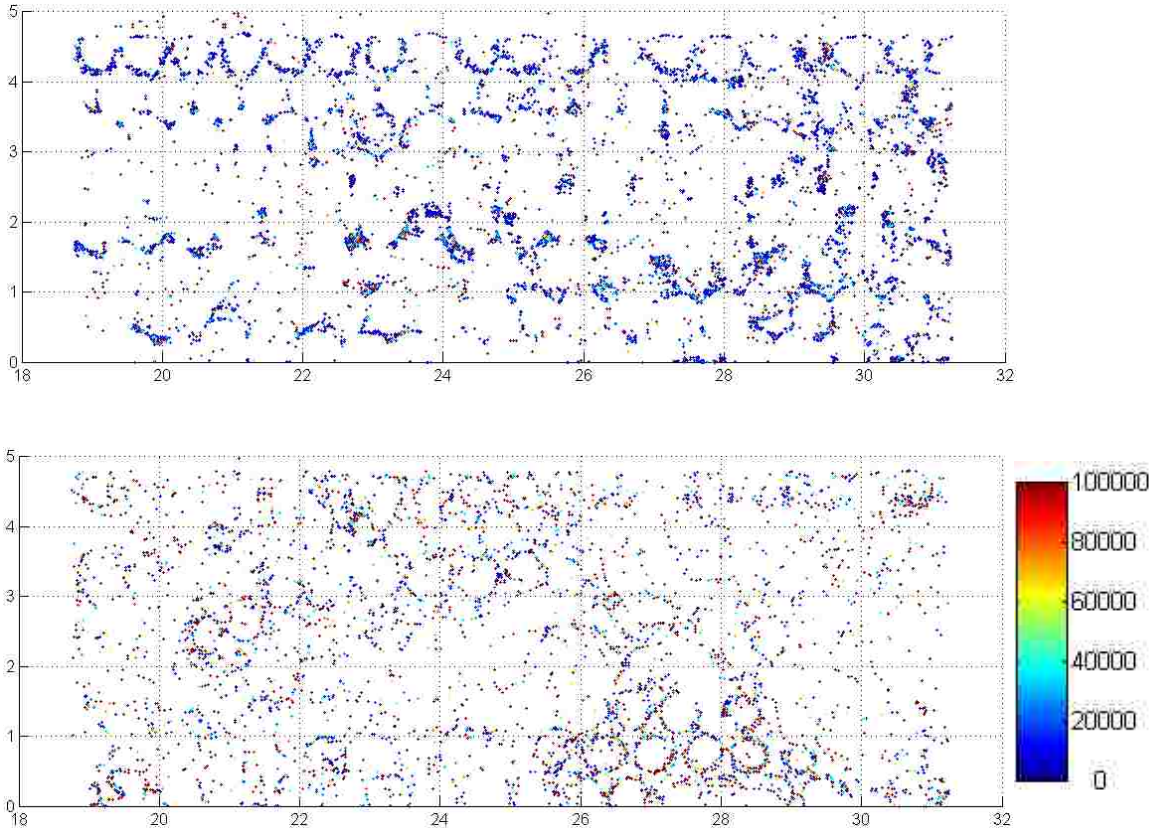

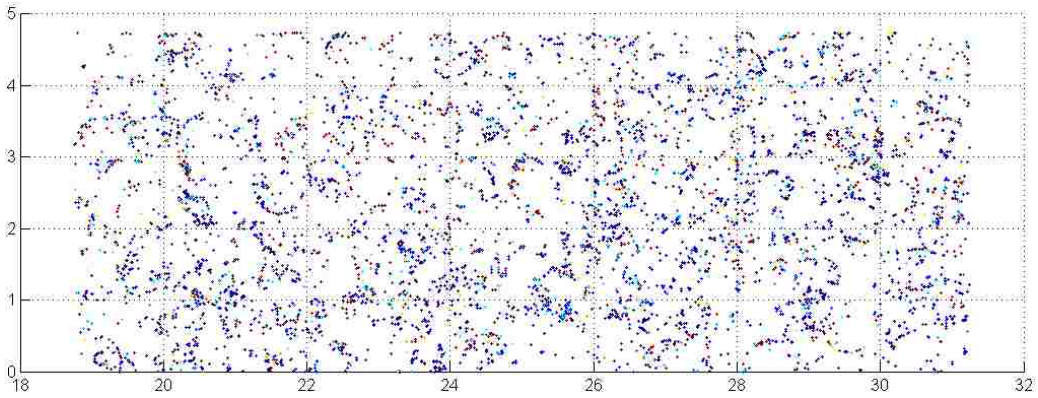

Figure 15. Distribution of detected fluorescence from attached nanoparticles at 3mM NaCl, pH 7.0, 350 PV of 0.00025 %solids nanoparticle suspension of (A) spherical particles, 1:1 (B) Rod-shape, 2:1 and (C) Rod-shape, 4:1, followed by 10 PV of background solution.

4. Summary

The influence of nanoparticle shape was studied using spherical latex particles (average diameter of 210 nm) and rod-shape particles, which were stretched from the spherical particles to aspect ratios of 2:1 and 4:1. The ζ-potential of the particles became less negative with increasing aspect ratios. This change in ζ-potential might be attributed to residual PVA left on the surface of the stretched rod-shape particles. The deposition rates of spherical and rod-shape were studied under favorable conditions using QCM-D and PLL-coated silica sensor surfaces with various ionic strengths ranging from 3 to 100 mM NaCl and 0.1 to 10 mM $CaCl_2$. Spherical particles were found to have a greater deposition rate compared to rod-shape particles and decreased with increasing ionic strength whereas the rod-shape particles were not sensitive to the changes in ionic strength. Flow cell experiments conducted with LSC found rod-shape particles had a faster attachment rate compared to spherical particles. It was also found that physical and chemical heterogeneities on the beads surface play a significant role in the attachment of particles onto the glass beads. Considerable differences in nanoparticle attachment and

deposition for spherical and rod-shape particles were found in this study. Flow cell experiments conducted using LSC proved to be an insightful tool for investigation the transport and attachment behaviors or nanoparticles in saturated porous media. Some additional experiments may be required to ensure the changes in surface charge of the original and stretched particles were not the driving force behind the changes in attachment rates. It is likely that a combination of physicochemical and hydrodynamic forces that determine the fate and transport of various shaped particles in porous media.

Reference

Adamczyk, Z., Weronski, P., 1998. Adsorption of nonspherical particles at solid/liquid interfaces. Croatica Chemica Acta. 71 (4), 949-974.

Auset, M., Keller, A. A., 2004. Pore-scale processes that control dispersion of colloids in saturated porous media. Water Resour. Res. 40, W03503.

Baltus, R. E., Badireddy, A. R., Xu, W., Chellam, S., 2009. Analysis of configurational effects on hindered convection of nonspherical bacteria and viruses across microfiltration membranes. Ind. Eng. Chem. Res. 48 (5), 2404-2413.

Ben-Moshe, T., Dror, I., Berkowitz, B., 2010. Transport of metal oxide nanoparticles in saturated porous media. Chemosphere 81 (3), 387-393.

Champion, J. A., Katare, Y. K., Mitragotri, S., 2007. Making polymeric micro- and nanoparticles of complex shapes. Proceedings of the National Academy of Sciences 104 (20), 11901-11904.

Chen, K. L., Elimelech, M., 2006. Aggregation and deposition kinetics of fullerene (C60) nanoparticles. Langmuir 22 (26), 10994-11001.

Chen, K. L., Elimelech, M., 2008. Interaction of fullerene (C60) nanoparticles with humic acid and alginate coated silica surfaces: measurements, mechanisms, and environmental implications. Environ. Sci. Technol. 42 (20), 7607-7614.

Elimelech, M., 1991. Kinetics of capture of colloidal particles in packed beds under attractive double layer interactions. J. Colloid Interface Sci. 146 (2), 337-352.

Elimelech, M., 1994. Effect of particle size on the kinetics of particle deposition under attractive double layer interactions. J. Colloid Interface Sci. 164, 190-199.

Guzman, K. A. D., Finnegan, M. P., Banfield, J. F., 2006. Influence of surface potential on aggregation and transport of titania nanoparticles. Environ. Sci. Technol. 40 (24), 7688-7693.

Ho, C. C., Keller, A., Odell, J. A., Ottewill, R. H., 1993. Preparation of monodisperse ellipsoidal polystyrene particles. Colloid Polym. Sci. 271, 469-479.

Ho, C. C., Ottewill, R. H., Yu, L., 1997. Examination of ellipsoidal polystyrene particles by electrophoresis. Langmuir 13, 1925-1930.

Ho, C. C., Ottewill, R. H., 1998. Investigation of the charge distribution of ellipsoidal particles. Colloids Surface A 141, 29-35.

Kuznar, Z. A., Elimelech, M., 2007. Direct microscopic observation of particle deposition in porous media: role of the secondary energy minimum. Colloids and Surfaces A: Physicochem. Eng. Aspects 294, 156-162.

Lecoanet, H. F., Bottero, J., Wiesner, M. R., 2004. Laboratory assessment of the mobility of nanomaterials in porous media. Environ. Sci. Technol. 38 (19), 5164-5169.

Litton, G. M., Olson, T. M., 1993. Colloid deposition rates on silica bed media and artifacts related to collector surface preparation methods. Environ. Sci. Technol. 27 (1), 185−193.

Liu, Q., Lazouskaya, V., He, Q., Jin, Y., 2010. Effect of particle shape on colloid retention and release in saturated porous media. Journal of Environmental Quality 39, 500-508.

May, R., Akbariyeh, S., Li, Y., 2012. Pore-scale investigation of nanoparticle transport in saturated porous media using laser scanning cytometry. Environ. Sci. Technol. 46 (18), 9980-9986.

Ponder, S. M., Darab, J. G., Mallouk, T. E., 2000. Remediation of Cr(VI) and Pb(II) aqueous solutions using supported, nanoscale zero-valent iron. Environ. Sci. Technol. 34 (12), 2564-2569.

Rajan, C. S., 2011. Nanotechnology in groundwater remediation. International Journal of Environmental Science and Development 2 (3), 182-187.

Salerno, M. B., Flamm, M., Logan, B. E., Velegol, D., 2006. Transport of rodlike colloids through packed beds. Environ. Sci. Technol. 40 (20), 6336-6340.

Toy, R., Hayden, E., Shoup, C., Baskaran, H., Karathanasis, E., 2011. The effects of particle size, density and shape on margination of nanoparticle microcirculation. Nanotechnology 22, 115101.

Wang, Y., Hammes, F., Düggelin, M., Egli, T., 2008. Influence of size, shape, and flexibility on bacterial passage through micropore membrane filters. Environ. Sci. Technol. 42 (17), 6749-6754.

Wang, C., Bobba, A. D., Attinti, R., Shen, C., Lazouskaya, V., Wang, L., Jin, Y., 2012. Retention and transport of silica nanoparticles in saturated porous media: effect of concentration and particle size. Environ. Sci. Technol. 46 (13), 7151-7158.

Weiss, T. H., Mills, A. L., Hornberger, G. M., Herman, J. S., 1995. Effect of bacterial cell shape on transport of bacteria in porous media. Environ. Sci. Technol. 29 (7), 1737-1740.

Xu, S., Liao, Q., Saiers, J. E., 2008. Straining of nonspherical colloids in saturated porous media. Environ. Sci. Technol. 42 (3), 771-778.

Yao, K., Habibian, M. T., O'Melia, C. R., 1971. Water and wastewater filtration: concepts and applications. Environ. Sci. Technol. 5 (11), 1105-1112.

Appendix A: Detailed Procedures

A.1. Polystyrene Nanoparticle Stretching Procedure

Spherical polystyrene particles with an average diameter of 220 nm were purchased from Polysciences, Inc. These spherical particles were manipulated from the spherical shape into rods shapes with an aspect ratio of 2:1 for use in studying the effects of shape on the transport and attachment of nanoparticles in porous media.

The first step to stretching the particles was to prepare the particles in an aqueous solution of polyvinyl alcohol (PVA) and dried into a solid film.

1. First, heat 40 mL MilliQ water in an 80 mL beaker to 80 ˚C.
2. Next, slowly pour 3.5 g PVA into the heated water. A 10% weight/volume (wt. /vol.) basis of PVA/water solution is desired, but some water evaporation is expected during the heating process. Once the PVA is poured into the heated water, it will take approximately 30 minutes for the PVA to completely dissolve.
3. After the PVA has been completely dissolved, turn the head off and add 100 mg of glycerol and 1 mL particles at 2.5% solids. Generally, a 0.04% wt/vol. basis of particles/water solution is desired. However, this can range up to 0.7% for smaller particles.
4. The solution was then poured through a 100 μm filter onto an aluminum plate with length of 12 cm and width of 12cm. The film was allowed to dry overnight or for at least 12 hours.

The next step involved the physical manipulation of the film and subsequent stretching of the particles in the film. This was done by heating the particles beyond their

glass temperature and stretching the films to create voids. The heated particles could then fill the voids and when the film was cooled, the particles would solidify.

5. First, a white mineral oil bath was heated to 125 ˚C (at or slightly above the glass temperature of the polystyrene particles, T_g = 120 ˚C).
6. The films was cut into separate 5 cm x 5cm squares and mounted into the stretching apparatus.
7. The distance needed to stretch the film to the desired aspect ratio was calculated and the stopper on the stretching apparatus was adjusted.
8. The stretchers were placed into the oil and allowed to sit for 5 minutes before actual stretching process.
9. Once the films were stretched, they were removed from the oil and allowed to cool at room temperature before the films were cut approximately 1 cm from the stretcher.

The final step in the stretching process involved the dissolving of the film and the extraction of the particles from the film. A series of centrifugation was used to "clean" the particles and remove any PVA that may have attached to the particles.

10. After films were cut off the stretchers, they were wiped with 100% Isopropyl alcohol (IPA) and placed in about 50 mL of 100% IPA. They were then placed on a shaker for at least 2 hours.
11. The films were removed from the IPA and placed in a 50 mL centrifuge tube with 24.5 mL of MilliQ water. They were placed in a water bath at 70 ˚C overnight or until all the films were dissolved.

12. Once they were completely dissolved, 10.5 mL of IPA was added to the centrifuge tube to make a 30% IPA/water solution. Next, they were vortex and sonciated for a total of 5 minutes.
13. The particles were then placed in the centrifuge for 90 minutes at 13,000 rpm and decanted afterwards.
14. This process was continued with decreasing amounts of IPA until 0% IPA. The solution was heated in a 70˚C water bath for the first four washing steps to ensure dissolution of IPA. See table below for reference.
15. Finally, the particles were suspended in 100% DI water and stored at 4 ˚C.

Washing Step	% IPA	Heat in 70˚C water bath	Centrifuge Speed (rcf)	Centrifuge Time (minutes)
1	30	1 hour	10,800	90
2	20	30 minutes	10,800	90
3	15	30 minutes	10,800	90
4	10	30 minutes	10,800	90
5	5	N/A	10,800	90
6	0	N/A	10,800	90
7	0	N/A	10,800	90

A.2. Glass Bead Washing Procedure

1. Place beads in beaker filled with pure Acetone solution and swirl to wash
2. Wash beads in pure Hexane solution
3. Soak beads for approximately 12 hours in 12.1 M HCl solution
4. Rinse several times with DI water to remove HCl
5. Sonicate beads in 0.01 M NaOH solution for 20 minutes at room temperature
6. Sonicate beads in DI water for 20 minutes at room temperature
7. Sonicate beads in 1.0 M HNO_3 for 20 minutes at room temperature

8. Rinse beads with DI water until pH reaches 7.0
9. Oven-dry the beads at 125˚C for 12 hours
10. Sieve beads with a size 25 U.S. sieve, resulting in a uniform distribution of beads of diameter between 600 to 710 μm.

A.3. Electrophoretic Mobility of Glass Beads Procedure

1. Weigh out 7 grams of glass beads
2. Sonicate the beads in 12 mL of electrolyte of interest
3. Collect liquid from sonicated beads
4. Dilute if necessary for use in ZetaSizer (Malvern Instruments)
5. Measure for mobility and ζ-potential in ZetaSizer

Appendix B: Interaction Energy Equations

Equations developed by Guzman et al. (2006) were used to estimate the interaction energy profile for spherical nanoparticle-plane (glass bead) van der Waals interaction and double layer repulsion.

Van der Waals (φ_{VDW}):

$$\phi_{VDW} = -\frac{A}{6}\left[\frac{a}{h} + \frac{a}{h+2a} + \ln\left(\frac{h}{h+2a}\right)\right]$$

Where: A is the Hamaker constant for the glass-water-latex system ($1x10^{-20}$, Tufenkji and Elimelch 2005), a is the average radius of the spherical nanoparticles, and h is the separation distance.

Double Layer Repulsion:

$$\phi_{EDL} = \pi\varepsilon_o\varepsilon_r k\left(\psi_s^2 + \psi_p^2\right)$$

Where: ε_0 is the permittivity of vacuum (8.85E-12 C2/N*m^2), ε_r is the relative dielectric constant of the medium (75), k is the inverse Debye length, and ψ_s *and* ψ_p are the surface potentials of the particle and glass bead surface, respectively.

$$\int_o^a \left(-coth\left[K\left(h+a-a\sqrt{1-\left(\frac{r}{a}\right)^2}\right)\right] + coth\left[K\left(h+a+a\sqrt{1-\left(\frac{r}{a}\right)^2}\right)\right] + \frac{2\psi_s\psi_p}{(\psi_s^2+\psi_p^2)}\left\{csch\left[K\left(h+a-a\sqrt{1-\left(\frac{r}{a}\right)^2}\right)\right] - csch\left[K\left(h+a+a\sqrt{1-\left(\frac{r}{a}\right)^2}\right)\right]\right\}\right) r dr$$

$$K^{-1} = \left(\frac{\varepsilon_o\varepsilon_r k_B T}{2e^2 1000 I_c N_A}\right)^{0.5}$$

Where: k_B is the Boltzmann constant (1.38×10^{-23} m^2 kg s^{-2} K^{-1}), T is temperature [K], N_A is the Avogadro constant (6.02×10^{23}), I_c is the ionic strength of the suspension, and e is the elementary charge (1.60×10^{-19}C).

Appendix C: Experimental Procedure Information

C.1 QCM-D Experimental Flow Chamber

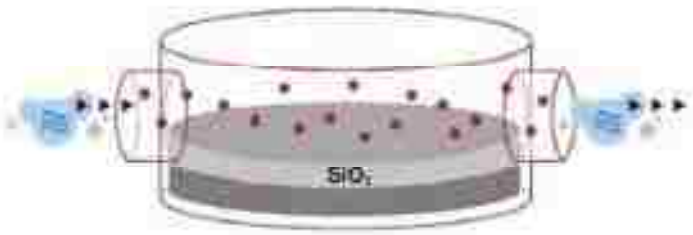

Figure C.1. QCM-D flow chamber (Chen & Elimelch, 2006)

Poly-L-lysine (PLL) Polyelectrolyte Modification of Silica Sensor:

The PLL solution was prepared with 10 mM N-(2-Hydroxyethyl) piperazine-N'-(2-ethanesulfonic acid) (HEPES, H4034, Sigma Aldrich, St. Louis, MO), 100 mM NaCl, and PLL (93.8 kDa, Sigma Aldrich, St. Louis, MO) at a concentration of 0.1 g/L. The "PLL-free" buffer solution consisted of 10 mM HEPES and 100 mM NaCl.

C.2 Flow Cell Schematic

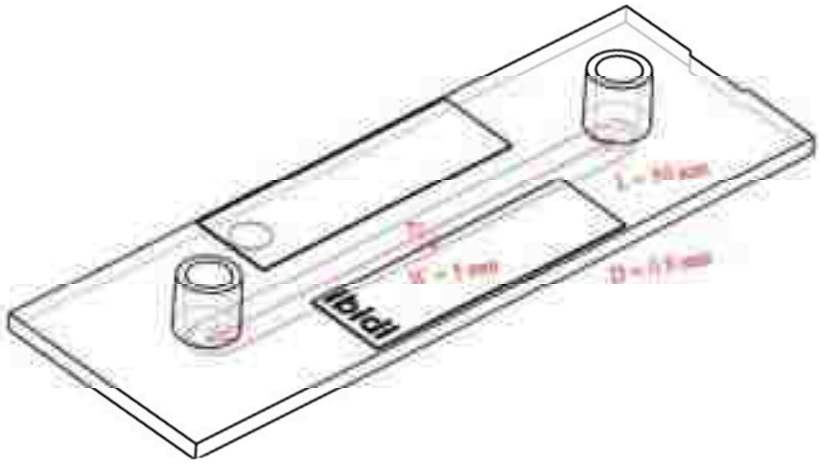

Figure C.2. Flow cell schematic (adapted from http://ibidi.com).

Appendix D: Instrumentation Photos

Figure D.1. Diffuse Reflectance Infrared Fourier Transform Spectroscopy (DRIFTS) Analysis.

Figure D.2. Raman Spectroscopic Analysis.

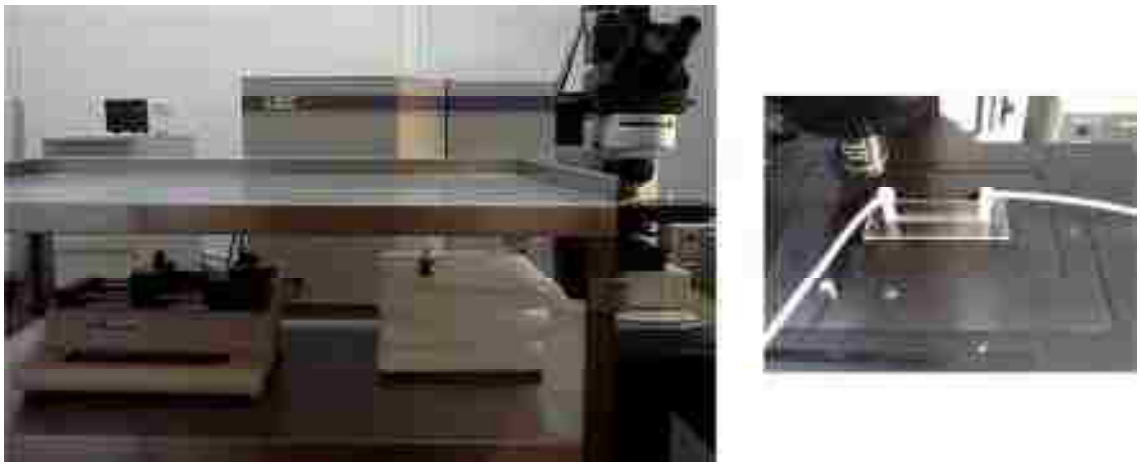

Figure D.3. Laser Scanning Cytrometry (LSC).

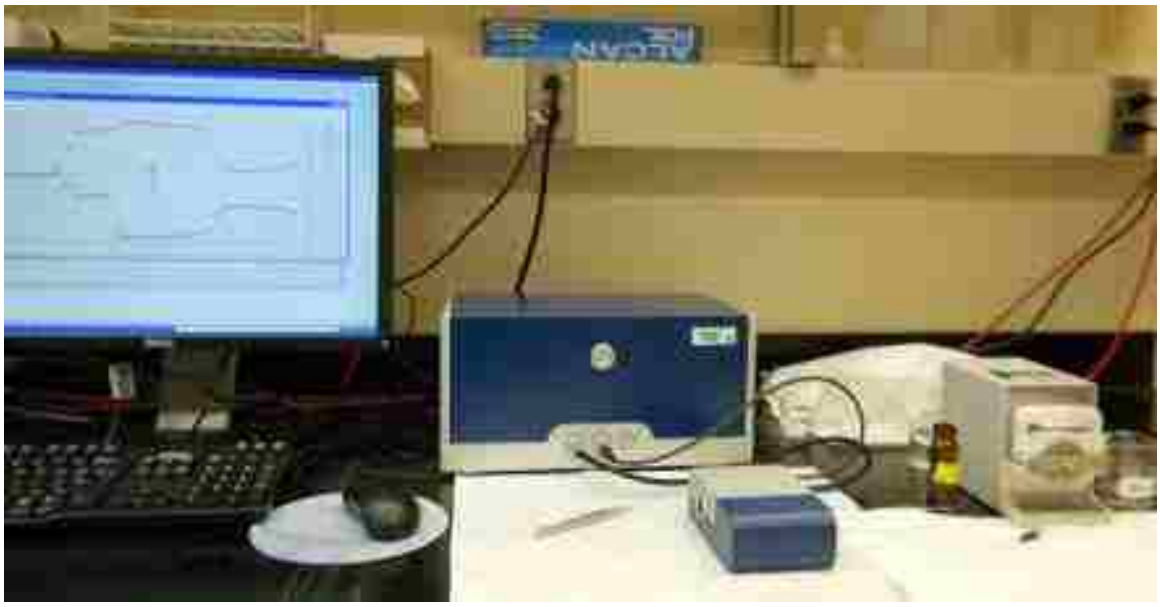

Figure D.4. Quartz Crystal Microbalance with Dissipation (QCM-D).

Figure D.5. Particle Stretching Apparatus.

Appendix E: LSC Flow Cell Scans

Spherical Particles (1:1) Scans for conditions of 3 mM NaCl and pH=7.0

10PV:

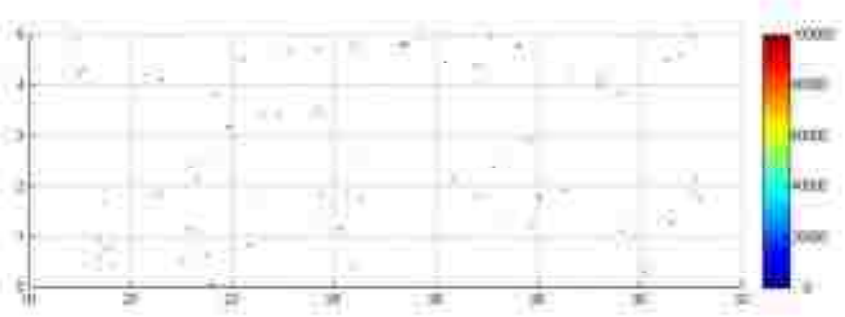

20 PV:

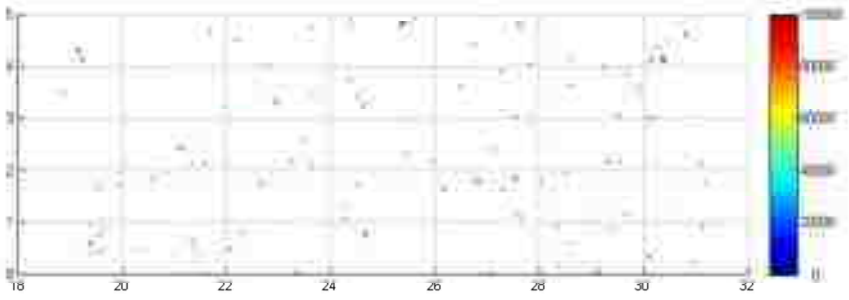

40 PV:

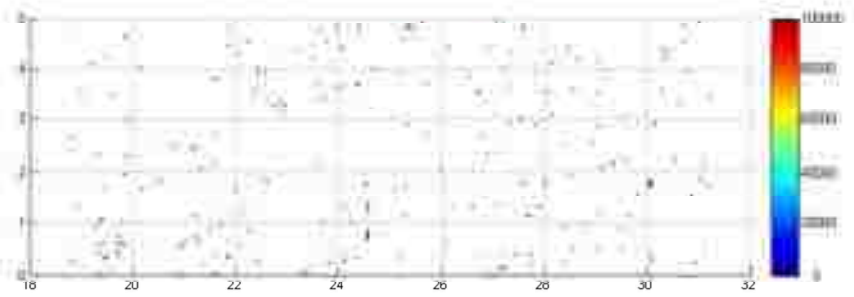
18
20
22
24
26
28
30
32

80 PV:

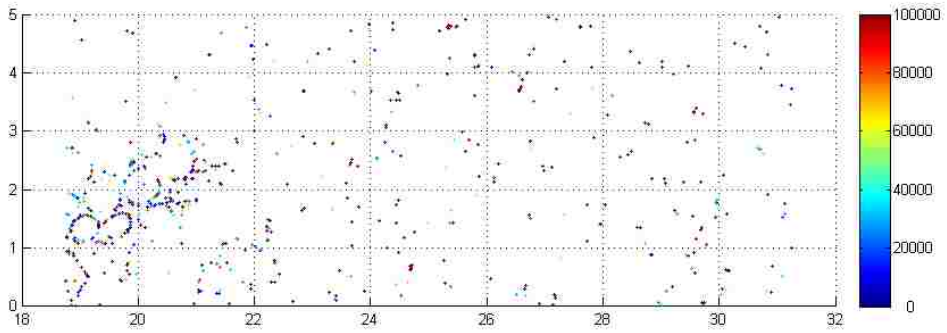
0
1
2
3
4
5
18
20
22
24
26
28
30
32
100000
80000
60000
40000
20000
0

Stretched rod-shape (2:1) scan at conditions of 3 mM NaCl & pH=7.0

10 PV:

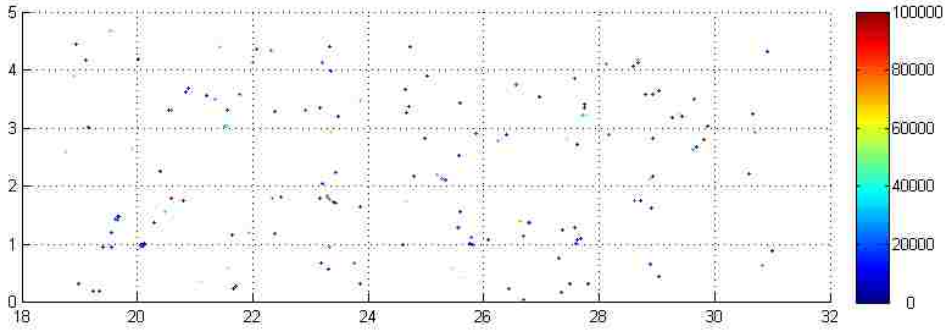

20 PV:

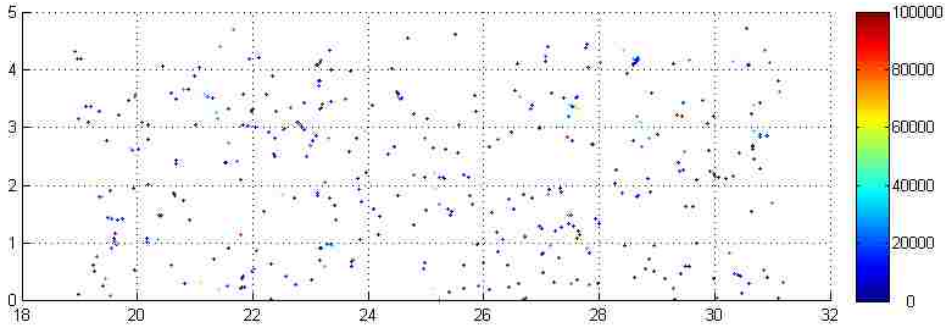

40 PV:

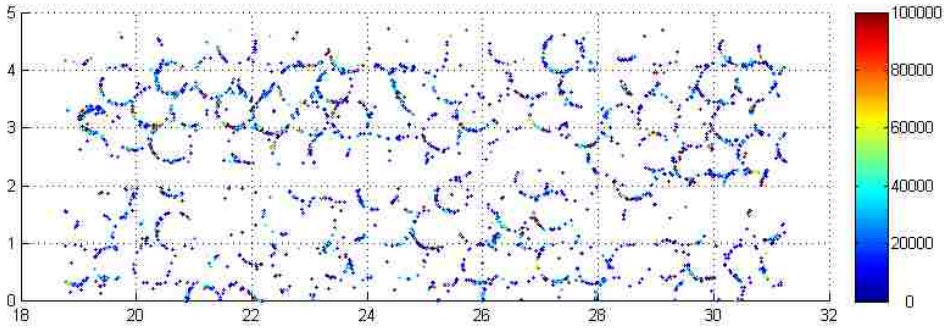
5
4
3
2
1
0
18
20
22
24
26
28
30
32
100000
80000
60000
40000
20000
0

80 PV:

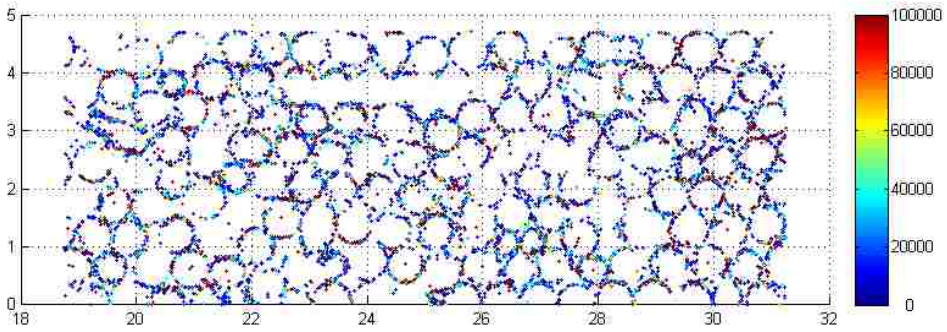
5
4
3
2
1
0
18
20
22
24
26
28
30
32
100000
80000
60000
40000
20000
0

Stretched rod-shape (2:1) Scans in conditions of 0 mM NaCl & pH=7.0

10 PV:

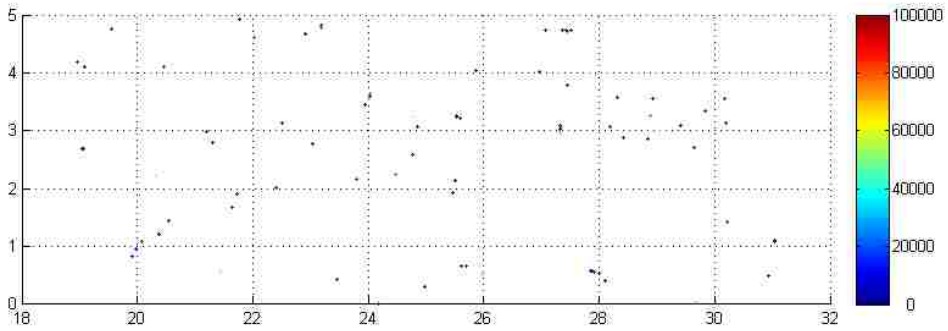

20 PV:

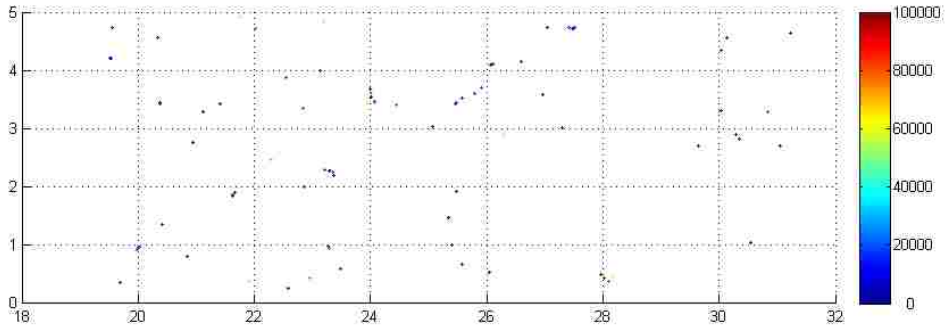

40 PV:

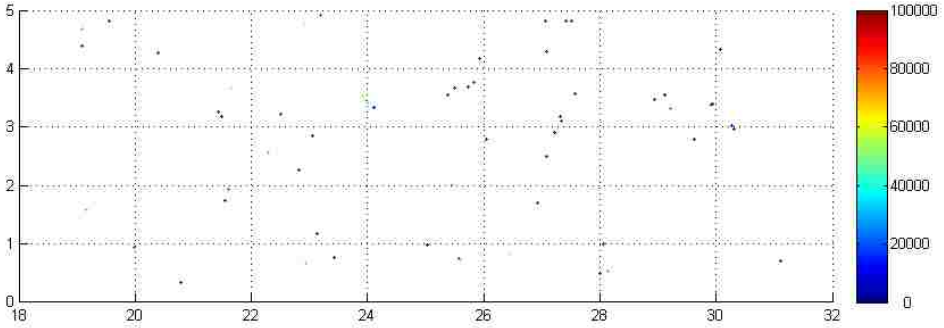
5
4
3
2
1
0
18
20
22
24
26
28
30
32
100000
80000
60000
40000
20000
0

80 PV:

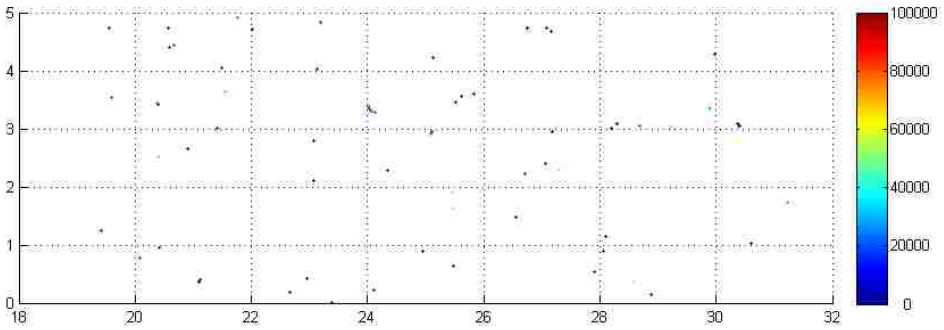
5
4
3
2
1
0
18
20
22
24
26
28
30
32
100000
80000
60000
40000
20000
0

Stretched rod-shape (2:1) Scans at conditions of 50 mM NaCl & pH=7.0

10 PV:

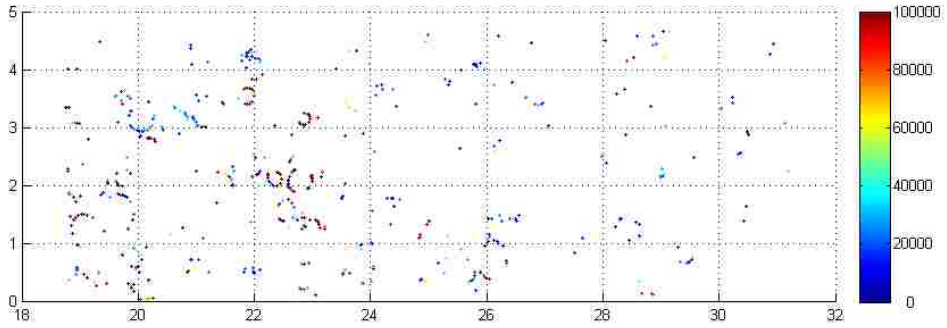

20 PV:

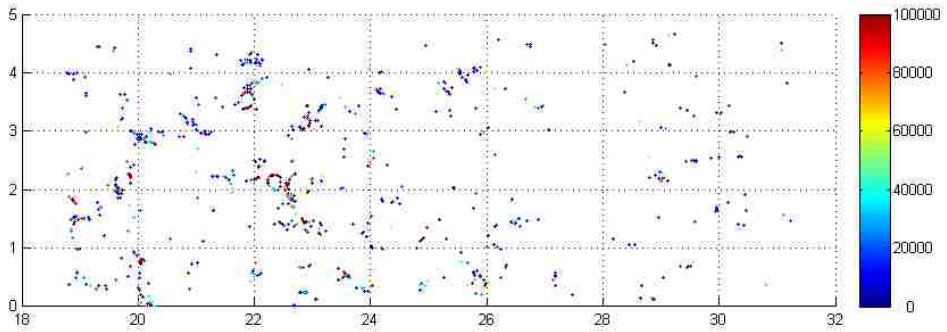

40 PV:

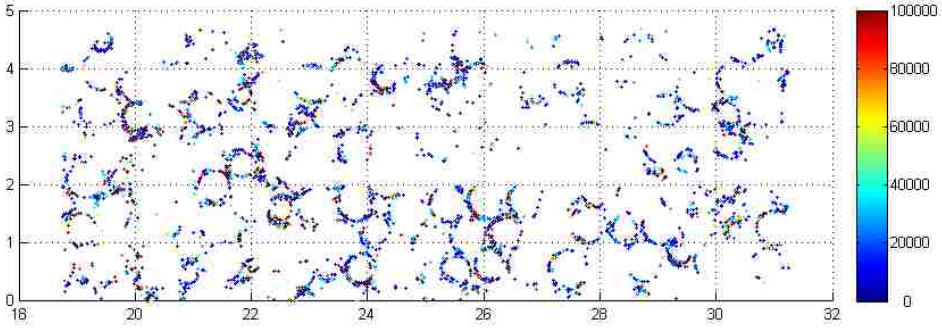
5
4
3
2
1
0
18
20
22
24
26
28
30
32
100000
80000
60000
40000
20000
0

80 PV:

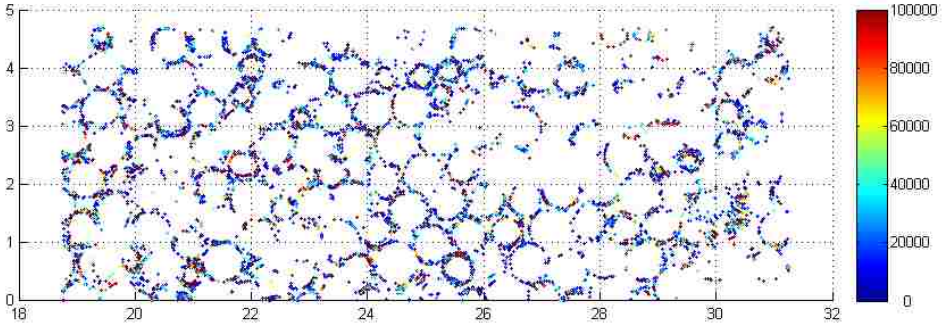
5
4
3
2
1
0
18
20
22
24
26
28
30
32
100000
80000
60000
40000
20000
0